

1 **Late Quaternary depositional and glacial history of the Arliss Plateau off the East**
2 **Siberian margin in the western Arctic Ocean**

3
4 Young Jin Joe^{1,2}, Leonid Polyak³, Michael Schreck^{1,4}, Frank Niessen⁵, Seok Hoon Yoon²,
5 Gee Soo Kong⁶, Seung-Il Nam^{1,*}
6

7 ¹Division of Polar Paleoenvironment, Korea Polar Research Institute, 21990 Incheon, Republic of Korea

8 ²Department of Earth and Marine Sciences, Jeju National University, 63243 Jeju, Republic of Korea

9 ³Byrd Polar and Climate Research Center, The Ohio State University, 1090 Carmack Road, Columbus, OH,
10 43210, USA.

11 ⁴Department of Geosciences, UiT-The Arctic University of Norway, N-9037 Tromsø, Norway

12 ⁵Alfred Wegener Institute (AWI) Helmholtz Centre for Polar and Marine Research, D- 27568 Bremerhaven,
13 Germany

14 ⁶Petroleum and Marine Division, Korea Institute of Geoscience and Mineral Resources, 34132 Daejeon,
15 Republic of Korea
16
17
18
19
20
21
22

23 *Corresponding Author: Seung-Il Nam (sinam@kopri.re.kr)
24

25 Keywords: Arctic Ocean sediments, Late Quaternary, glacial history, sediment facies, seismostratigraphy
26

27 **Abstract** Sedimentary stratigraphy and facies analysis along with seismostratigraphic and
28 multibeam bathymetry data are used to reconstruct the last glacial impact on the Arliss Plateau (AP)
29 and attendant sedimentation in the adjacent Chukchi Basin (CB) in the western Arctic Ocean off the
30 East Siberian margin. Sediment core ARA02B/16B-GC from the AP lower slope captures glacier-
31 related depositional history during the last estimated ca. 100 ka (Marine Isotope Stage (MIS) 1 to 5c)
32 based on regional lithostratigraphic correlation. The sedimentary record shows distinguishable
33 interglacial (interstadial) and glacial (stadial) patterns. The identified sedimentary facies reflect several
34 modes of glaciogenic deposition by drifting icebergs, suspension settling from turbid meltwater plumes
35 and/or detached underflows, and turbidity currents. Based on strong seismic reflectors related to
36 lithological boundaries, a downslope subbottom profile from AP to CB is divided into
37 seismostratigraphic units (SSU) 1 and 2 corresponding in the core record to MIS 1-3 and MIS 3-5c,
38 respectively. An acoustically transparent lens within SSU 2 correlates on the upper slope to debris lobes
39 downslope from the AP top covered by megascale glacial lineations. This geomorphic/sedimentary
40 pattern indicates a glacial erosional impact on the AP and proglacial deposition of eroded sediments on
41 the slope and in the basin. Based on the developed sediment stratigraphy and facies analysis, the last
42 debris lobe horizon was deposited in glacial/deglacial environments during late MIS 4 to early MIS 3.
43 The absence of similar glaciogenic debris lobes within SSU 1 indicates no direct glacial impact on the
44 AP during the Last Glacial Maximum (MIS 2). These results suggest that the last glacial erosion of the
45 AP occurred during or immediately after MIS 4, possibly related to major glaciation in northern Siberia
46 at ~50-70 ka.

47 1. Introduction

48 Over last two decades, multiple geophysical investigations along with sedimentary records
49 revealed that the Arctic East Siberian and Chukchi continental margins have been repeatedly glaciated
50 during the Pleistocene (Jakobsson et al., 2008, 2014; Polyak et al., 2007; Niessen et al., 2013; Dove et
51 al., 2014; O'Regan et al., 2017). In particular, streamlined glacial lineations and related diamicton
52 deposits identified by swath seafloor and subbottom profiling on the East Siberian margin, including
53 the adjacent part of the Mendeleev Ridge known as the Arliss Plateau (AP) (Fig. 1C), indicate the
54 repeated development of up to 1 km-thick marine ice sheets/ice shelves (Niessen et al., 2013). However,
55 the age framework for these glacial events, and thus, their relation to a broader paleoclimatic context,
56 is not well understood. Recently, Schreck et al. (2018) provided lithostratigraphic insight on glacial
57 impacts on the East Siberian margin in the Late Pleistocene, concluding that the last major regional ice
58 grounding occurred during MIS 4 to 3 (60-70 ka). This conclusion differs from the notion that this event
59 was coeval with the deepest glacial erosion on the Lomonosov Ridge in the central Arctic Ocean
60 (Jakobsson et al., 2016; O'Regan et al., 2017), which has been constrained to MIS 6 (Jakobsson et al.,
61 2001).

62 To better constrain the timing of ice grounding events and their spatial pattern, it is important to
63 link the geophysical records and sediment core stratigraphy. This task requires analyzing representative
64 sedimentary records accompanied by sub-bottom seismic profiles and detailed multibeam bathymetry
65 from the areas affected by glaciations. However, most areas of continental margins, as well as
66 bathymetric highs on the oceanic ridges and plateaus impacted by glacial erosion or iceberg turbation,
67 are unsuitable for recovering well preserved, stratigraphically coherent records (Polyak et al., 2007;
68 Jakobsson et al., 2008; Dove et al., 2014). In comparison, the adjacent slopes and basins may hold more
69 expanded, better-preserved stratigraphies, provided their depositional context, which is sufficiently
70 constrained by geophysical data. In particular, the slope of the AP and the adjacent Chukchi Basin (CB)
71 was chosen for this study as a relatively well surveyed area of deposition for glaciogenic material
72 originating from the East Siberian continental margin (Niessen et al., 2013; Jakobsson et al., 2014;
73 Schreck et al., 2018). We are using a sediment core collected on a CHIRP sub-bottom **profile** (SBP)
74 from the AP top to the CB (Fig. 1) to reconstruct the depositional history of the East Siberian margin
75 during and since the last glacial grounding event.

76

77 **2. Regional setting**

78 **2.1. Seafloor morphology and sedimentary cover**

79 The CB is bounded by the Mendeleev Ridge/AP and the Chukchi Plateau and shelf and is
80 connected to the north with the Canada Basin (Fig. 1). The CB covers ~43,000 km² (Jakobsson et al.,
81 2003) and has a relatively flat and smooth seafloor ranging from 1,800 m to 2,300 m water depth and
82 comprised of well-stratified deposits (Dove et al., 2014). The tops of both the Arliss and the Chukchi
83 plateaus are covered by streamlined morphological features interpreted as megascale glacial lineations
84 (MSGSL), complicated in some areas with transverse ridges (Niessen et al., 2013; Dove et al., 2014;
85 Jakobsson et al., 2014, 2016). The outer parts of the East Siberian and Chukchi margins at water depths
86 to 700 m feature extensive till wedges and recessional moraines related to repeated glacial advances
87 and retreats (Niessen et al., 2013; Dove et al., 2014; Jakobsson et al., 2014). Further downslope these
88 margins as well as adjacent borderlands, including the AP, hold large, lens-shaped debris lobes (Fig. 2),
89 similar to seismostratigraphic features observed in the glacial trough mouth fans in front of large ice
90 streams (Batchelor and Dowdeswell, 2014; Jakobsson et al., 2014; O'Regan et al., 2017).

91

92 **2.2. Sediment stratigraphy in the western Arctic Ocean**

93 The Quaternary western Arctic sediments are generally characterized by the cyclical pattern of
94 dark brownish and olive/greyish units (Phillips and Grantz, 1997; Polyak et al., 2004, 2009; Adler et
95 al., 2009; Stein et al., 2010; Schreck et al., 2018). This color contrast was shown to be controlled by the
96 content of manganese (Mn) oxy(hydr)oxides, with higher values in brown units attributed to Mn inputs
97 from the continental margins at higher sea levels during interglacial/major interstadial periods
98 (Jakobsson et al., 2000; Polyak et al., 2004, 2009; März et al., 2011; Löwemark et al., 2014; Ye et al.,
99 2019). While Mn-enriched intervals can be affected by diagenetic remobilization and redistribution of
100 this redox-sensitive element, their stratigraphic pattern is consistent throughout the central Arctic Ocean

101 (März et al., 2011; Löwemark et al., 2014; Schreck et al., 2018). Their correlation is corroborated in
102 multiple cores by the distribution of other lithostratigraphic parameters, such as sediment density, ice-
103 rafted debris (IRD), and biogenic proxies. The brown, Mn-enriched units (layers), interpreted as
104 interglacial/major interstadial sedimentary intervals, are typically characterized also by low to moderate
105 amounts of coarse IRD, intense bioturbation, and relatively abundant microfossils (Polyak et al., 2004,
106 2009; Adler et al., 2009; Stein et al., 2010; Löwemark et al., 2012). In comparison, olive/greyish, Mn-
107 depleted units, related to glacial periods, are composed of fossil-poor sediments with strongly variable
108 IRD amounts (Polyak et al., 2004, 2009; Adler et al., 2009; Stein et al., 2010). Fine-grained and IRD-
109 rich lithological types of grey sediments have been attributed to glacial maxima and deglacial
110 depositional environments, respectively. At sites proximal to glaciated areas, deglacial sediments may
111 have expanded thicknesses indicative of high depositional rates (Polyak et al., 2007; Wang et al., 2013;
112 Schreck et al., 2018). Some of the IRD peaks have characteristic sediment compositions used as
113 provenance indicators. In particular, detrital carbonates (mostly dolomites) are related to the Paleozoic
114 platform of the Canadian Arctic eroded by the Laurentide Ice Sheet (LIS) (Bischof and Darby, 1997;
115 England et al., 2009; Polyak et al., 2009; Stein et al., 2010; Bazhenova et al., 2017; Dong et al., 2017).
116 Peaks of this material forming characteristic pinkish-white (PW) layers in sediment cores (Clark et al.,
117 1980) can be used to track the distribution of icebergs in the Arctic Ocean during the LIS collapse events.

118

119 **3. Material and methods**

120 **3.1. Material**

121 We use a 378-cm-long, 12-cm in diameter gravity sediment core ARA02B/16B-GC (hereafter
122 16B-GC) and high frequency (2.5-6.5 kHz) subbottom CHIRP profiler data collected on the AP slope
123 (Fig. 1) during the 2nd RV *Araon* Arctic Expedition (ARA02B) in 2011. Multibeam bathymetry
124 mapping of the AP top (Fig. 1C) was subsequently conducted in 2012 (ARA03B). The 16B-GC coring
125 site (76° 24' N, 175° 58' W, 1841 meter water depth (mwd)) was selected based on the AWI Parasound
126 data acquired previously on the 2008 RV *Polarstern* Arctic expedition ARK-24/3 (Jokat, 2008). The

127 site is located ~1 km downslope from the foot of glaciogenic debris lobes and features relatively flat
128 and smooth seafloor with acoustically well stratified subbottom reflectors (Fig. 2). A 38-cm-long box
129 core 16B-BC was taken at the same site to recover the surficial sediment. Based on the comparison with
130 16B-BC, about 10 cm of top sediment is lost in 16B-GC, including the surficial brown lithological unit
131 B1, which was spliced for a composite record of 16B-BC (Figs. 3, 4).

132

133 **3.2. Methods**

134 After a visual description of the split core, its line-scan images and elemental geochemistry were
135 acquired with AVAATECH XRF-core scanner at Korea Institute of Geoscience and Mineral Resources
136 (KIGAM). Line-scanning was conducted using a Jai CV L107 camera with red-green-blue (RGB)
137 channels. L* (lightness) and a* (red-green color space) data were used for correlation with previously
138 published sediment records (Schreck et al. 2018). Sediment elemental composition was measured at 5-
139 mm intervals using X-ray fluorescence (XRF) AVAATECH scanner settings reported in Schreck et al.
140 (2018). Mn and calcium (Ca) XRF data used in lithostratigraphic correlation were normalized to
141 aluminum (Al) to eliminate the potential dilution effect of background sedimentation (e.g., März et al.,
142 2011). We note, however, that Mn and Ca variations in Arctic sediments are largely independent of the
143 background lithogenic elements as shown in prior studies (e.g., Löwemark et al., 2014; Dong et al.,
144 2017)

145 X-radiographs were performed for detailed sediment structure on 1 x 10 x 30 cm slabs. X-ray
146 images were taken with SOFTEX m-100w digital x-ray scanner (EZ-320) and instantly processed using
147 iX-Pect X-Ray imaging software. Darker objects in X-radiographs presented in this study display dense
148 material, such as lithic fragments. Coarse debris >2 mm in diameter was counted at every 1 cm,
149 according to Grobe (1987). Samples for sediment texture were taken at 10 cm intervals and treated with
150 35% H₂O₂ to decompose organic matter. Sand-sized and coarser grains were separated by wet sieving
151 at 63 µm and dry sieving at 2 mm standard sieves. The grain size of <63-µm sediment was measured
152 with a Micromeritics Sedigraph 5000D.

153 The multibeam bathymetric survey was performed using a hull-mounted EM122 echosounder.
154 Acquired bathymetric data were processed onboard using a specialized software CARIS. Sub-bottom
155 seismic-reflection data were acquired with the CHIRP SBP-120 profiler with the vertical resolution on
156 the 10 cm scale in acoustically stratified sediments. The SBP data were logged in the TOPAS raw
157 format, which was converted to an SEG-Y format and allowed for post-processing with standard
158 software packages. The estimated sound velocity of 1500 m/s was used to convert the signal travel time
159 into sediment depth for comparison with core lithostratigraphy.

160

161 **4. Results**

162 **4.1. Lithostratigraphy**

163 Core 16B is composed of sandy to fine-grained mud displaying a general cyclic depositional
164 pattern characterized by an alternation of brown to dark brown and yellow to olive greyish sedimentary
165 units (Figs. 3, 4). The concentration of coarse IRD (>2 mm) increases at lithological boundaries and
166 within some brown units, whereas IRD within yellow to olive greyish units is typically rare.

167 A total of five Mn-rich brown units, B1 to B5, are identified in the recovered stratigraphy based
168 on sediment color, and Mn/Al ratio (Fig. 3) along with sedimentary structure and texture (Fig. 4),
169 including the upper unit B1 spliced from the box core 16B-BC. The brown units show a characteristic
170 low-L* (darker) and high-a* (more reddish) color pattern with a relatively symmetrical distribution
171 across each unit (Fig. 3). High Mn/Al ratios in surficial sediments may be partially due to high water
172 content (Thallingii et al., 2007), but that does not affect the stratigraphic distribution of Mn values,
173 which are high in unit B1. The brown units mostly consist of slightly sandy mud with scattered IRD
174 and have relatively sharp upper boundary and uneven, bioturbated (mottled) lower boundary (Fig. 4).
175 Yellowish to olive-grey units are generally thicker than brown units and are mostly composed of fine-
176 grained mud without coarse IRD. In particular, the second grey unit between B2 and B3 is the thickest
177 interval recovered (~150 cm) with a consistent lithology. Two PW carbonate layers, consisting of

178 sandy-gravelly mud and expressed as relatively solid lenses and adjacent scattered speckles, are
179 identified above B2 and at the base of B3, corresponding to prominent Ca/Al peaks (Figs. 3, 4).

180

181 **4.2. Sediment facies**

182 Sediment of core 16B was classified into five major facies based on sedimentary structure,
183 texture, and color (Fig. 4, Table 1): bioturbated sandy mud (Bsm), bioturbated mud (Bm), crudely
184 laminated or layered mud (CLm), thinly laminated mud/muddy sand (TLm/TLs), and homogeneous
185 mud (Hm).

186 Bioturbated sandy mud (Bsm) is mostly identified in brown units and PW carbonaceous layers
187 and is characterized by strong bioturbation overprinting primary sedimentary structures, sharp upper-
188 and uneven, mottled lower-boundaries (Fig. 4). This facies mainly consists of very poorly sorted (2 – 4
189 Φ) sandy mud with coarse particles randomly scattered within the fine matrix (Fig. 3). In comparison
190 with the brown units, Bsm in the PW layers contains higher sand content, up to 22% (Fig. 3), and more
191 coarse particles.

192 Bioturbated mud (Bm) generally occurs at the transitions between brown and olive-grey units
193 and is characteristic for the olive-grey units underlying B1, where Bm is interbedded with the crudely
194 laminated or layered mud facies (CLm), and below B3 (Fig. 4). Similar to Bsm, the Bm facies also has
195 a mottled structure but is composed of more fine-grained muds with gradual facies boundaries. The
196 sediment sorting index in this facies (1 – 1.5 Φ) is lower than in Bsm due to a lack of coarse particles
197 (Figs. 3, 4).

198 Crudely laminated or layered mud (CLm) is characterized by the alternation of planar to sub-
199 parallel silt-and clay-rich laminae or layers with weak bioturbation (Fig. 4). Individual laminae are
200 generally difficult to discern. Clayey laminae/layers are mostly thicker (4 – 12 mm) than their silt-rich
201 counterparts (1 – 3 mm). Vertical changes in lamina thickness and composition appear to be random,
202 and the sediment is overall weakly sorted (1 – 1.5 Φ). Facies CLm is predominant within the second

203 olive-grey unit bounded by B2 and B3 and is also interbedded with the Bm facies in the first olive-grey
204 unit.

205 Thinly laminated mud/muddy sand facies (TLm/TLs) can be subdivided into silt-rich mud (TLm)
206 and muddy sand (TLs). This distinct facies has a laterally continuous lamination (a few millimeters
207 thick), typically identified as couplets with overlying homogeneous mud facies Hm (Fig 4). TLm/TLs
208 laminae show sharp lower and gradational upper boundaries, and relatively regular thicknesses (Fig. 3).
209 TLm/TLs facies occur episodically in the second and third olive-grey intervals, between B2 – B3 and
210 B3 – B4, respectively (Figs. 3, 4).

211 Homogeneous mud facies (Hm) consists of fine-grained muddy sediment characterized by an
212 overall absence of primary structures, bioturbation, or any grading. This facies is mostly interbedded
213 with the thinly laminated facies TLm/TLs on millimeter scales as couplets. Independently occurring
214 Hm facies (3 cm thick) is identified only in the upper part of the third olive-grey interval below B3 (Fig.
215 4).

216

217 **4.3. Geomorphology and seismostratigraphy of the AP basinward slope**

218 The seafloor of the AP top shows several sets of streamlined morphological features (Fig. 1C)
219 interpreted in prior studies as megascale glacial lineations (Niessen et al., 2013; Jakobsson et al., 2016).
220 The youngest set of lineations of SSW-NNE orientation is traced to water depths of ~950 m in the
221 southern part of AP, compared to somewhat shallower depths of 850 m in the northern part. The lineated
222 surface is covered by ~3-m thick, acoustically stratified sediment (Niessen et al., 2013).

223 The subbottom data from the basin-ward middle to the lower slope of the AP (~1600-1800 mwd)
224 show stacked series of debris lobes of ~10-20 km long and up to 25 m thick (Fig. 2A). The debris
225 deposits are covered by acoustically stratified sediments (Figs. 2B, C). Three distinct acoustic reflectors
226 (R1 – R3) were identified by lateral continuity and strong reflectivity. The reflectors divide the upper
227 part of the sediment cover into two major seismostratigraphic units, SSU 1 and 2.

228 The surficial unit SSU 1 bounded by reflectors R1 (seafloor) and R2 is laterally continuous and
229 has bedding parallel to R2 (Figs 2B and C). SSU 1 is characterized by transparent to slightly fuzzy sub-
230 bottom echoes, with a laterally discontinuous, weak reflector also recognized within this unit (Fig. 2B).
231 SSU 1 thins out from the core 16B site towards the steep middle slope (Figs. 2B and C) and is
232 indistinguishable further up-slope near the AP top.

233 As seen on records from the basin and lower slope (Fig. 2B), the underlying unit SSU 2, bounded
234 by R2 and R3, is generally characterized by parallel lamination with variable amplitudes and transparent
235 acoustic signature in the middle part of the unit. Further up-slope, two coeval debris lobes are
236 recognized in the lower part of SSU 2, covered by acoustically stratified sediment comprised of the
237 remaining part of SSU 2 and overlying SSU 1 (Figs. 2B, C). Two thin reflectors with low to moderate
238 reflectivity are identified in the lowermost part of SSU 2 in the basin, but cannot be found near the
239 debris lobes on the upper slope (Fig. 2B).

240

241 **5. Discussion**

242 **5.1. Age model**

243 As core 16B-GC lacks calcareous material for ^{14}C dating, its age model is constrained by
244 lithostratigraphic correlation with the earlier investigated core ARA03B/28B-GC from the AP top
245 (Schreck et al., 2018) and core HLY0503-8JPC from the foot of the Mendeleev Ridge ~350 km north
246 (Adler et al., 2009). The latter core record has the best regional age control constrained by multiple ^{14}C
247 datings in the upper part of the stratigraphy (MIS 1 to 3, units B1-B3), ^{14}C -calibrated amino-acid
248 racemization (AAR) rates extending to MIS 5 (Kaufman et al., 2008; Adler et al., 2009), and coccolith
249 occurrences (Backman et al., 2009). The correlation is primarily based on sediment color and
250 distribution of Mn and Ca content showing a regionally consistent pattern (Fig. 5) (Polyak et al., 2009;
251 Stein et al., 2010; Schreck et al., 2018). According to ^{14}C dating, brown, Mn-rich units B1 and B2,
252 including the detrital carbonate layer W3, represent MIS 1 (~ 9 ka) and MIS 3 (34-45 ka)
253 interglacial/interstadial environments, respectively (Fig. 5; Table 2). The intermittent grey unit G1 thus

254 corresponds to the last glaciation/deglaciation (MIS 2 to 1) and the youngest, pre-glacial part of MIS 3.

255 Brown units B3 to B5 recovered by core 16B-GC have been attributed in the reference cores to
256 pre-MIS 3 interstadials ranging to MIS 5c, with some variance. Based on coccolith distribution in
257 HLY0503-8JPC, Backman et al. (2009) suggested that B5 represents MIS 5a, while Adler et al. (2009)
258 assigned its age to MIS 5c, consistent with AAR ages (Kaufman et al., 2008). This age model was also
259 used by Schreck et al. (2018), who pointed out that the coccolith stratigraphy cannot pinpoint a specific
260 time interval within MIS 5. In any case, core 16B-GC does not reach the prominent detrital carbonate
261 layer PW2 identified in multiple cores across the western Arctic Ocean, including HLY0503-8JPC (Fig.
262 5), and attributed to MIS 5d (e.g., Stein et al., 2010; Bazhenova et al., 2017; Dong et al., 2017). Overall,
263 we consider MIS 5c, with the approximate age of ca. 100 ka, as a reasonable estimate for the bottom of
264 16B-GC.

265 The developed lithostratigraphic framework indicates that a ~150-cm thick grey unit G2 pre-
266 dates the MIS 3 interstadial, likely being contained in the time interval from MIS 4 to early MIS 3. This
267 prominent lithostratigraphic unit can be traced in multiple cores from the Siberian margin to the Arctic
268 Ocean interior (e.g., Spielhagen et al., 2004; Polyak et al., 2009; Dong et al., 2017; Wang et al., 2018),
269 and has been proposed to correlate to the last pre-LGM glaciation in northern Eurasia with a glacial
270 maximum around 50-60 ka (Svendsen et al., 2004).

271 In comparison to this, regionally consistent age model, the B2 unit in a very similar nearby record
272 was assigned to MIS 5 based solely on the presence of rare coccoliths, including *E. huxleyi* (core
273 SWERUS-L2-13PC; <https://bolin.su.se/data/swerus/physical.php>; Fig. 1) (Jakobsson et al., 2016). **The**
274 **occurrence of *E. huxleyi* clearly indicates that the sediments of this unit are younger than MIS 8/7**
275 **(Thiersten et al., 1977; Backman et al., 2009). However, due to an overall limited occurrence of**
276 **coccoliths, *E. huxleyi* presence may not be used to identify specific substages within MIS 5 as**
277 **attempted previously (e.g., Jakobsson et al., 2001; Spielhagen et al., 2004) because this species can**
278 **potentially occur in other relatively warm intervals of Arctic sediments.** In particular, MIS 3 is a very
279 pronounced interstadial unit in Arctic paleoceanographic records, as exemplified by a high content of

280 Mn and high productivity indicated by abundant planktic and benthic microfossils (Nørgaard-Pedersen
281 et al., 1998; Adler et al., 2009; Hanslik et al., 2010; Schreck et al., 2018). Some authors further inferred
282 reduced sea ice and enhanced the advection of Atlantic waters during this time (Cronin et al., 2012;
283 Poirier et al., 2012). We note that in another SWERUS core from the Siberian margin further west, *E.*
284 *huxleyi* was also found in B2 with a ¹⁴C age of 33 ka just a little above this finding (O'Regan et al.,
285 2017).

286

287 5.2. Core-seismic correlation

288 Distinct acoustic reflectors on seismic records can be formed by vertical changes in acoustic
289 impedance controlled by sediment density and p-wave velocity. Deep-sea Arctic Ocean sediments
290 generally consist of relatively soft fine-grained muds, which are occasionally intercalated with denser,
291 coarse sediment layers mostly attributed to iceberg sedimentation during deglacial events (Clark et al.,
292 1980; Polyak et al., 2009; Stein et al., 2010; Dong et al., 2017; Schreck et al., 2018). In particular,
293 detrital carbonate IRD layers, such as W3 and PW2 captured by western Arctic Ocean sediments, are
294 characterized in cores from the study region by a remarkably high density and p-wave velocity
295 compared to the enclosing fine-grained muds (Matthiessen et al., 2010; Stein et al., 2010; Schreck et
296 al., 2018). These layers, marking the LIS iceberg discharge from the Canadian Arctic, thus have the
297 potential to form strong reflectors.

298 Comparison of the subbottom acoustic reflection data and core 16B record (Fig. 6) confirms that
299 the surficial reflector R1 represents the seafloor, the interface between bottom water and relatively dense
300 surficial sediment of unit B1. A fine-grained unit G1 characterized by a relatively constant density and
301 p-wave velocity in multiple records from the study region (Matthiessen et al., 2010; Stein et al., 2010;
302 Schreck et al., 2018) defines a mostly transparent echo characteristic of SSU 1. A strong reflector R2
303 probably indicates a pronounced lithological change from the IRD-rich interval, including the W3 layer
304 to the overlying fine-grained unit G1 (Fig. 6). A relatively strong reflector in the uppermost part of SSU
305 2, partially divided into two layers, appears to be associated with a relatively coarse unit B2 (Fig. 6). A

306 transparent echo signature similar to that in SSU 1 characterizes the upper part of SSU 2 corresponding
307 to the fine-grained, thickest unit G2. Two thin reflectors of low to moderate amplitude in the lower part
308 of SSU 2 appear to correspond to a relatively sandy unit B3, especially its detrital carbonate-rich base
309 layer, and an intermittent sandy layer within G3 (Fig. 6). While core 16B-GC does not extend to the
310 depth of R3, a likely candidate for this strong reflector is a prominent, IRD-rich, detrital carbonate layer
311 PW2 that underlies unit B6 and is barely reached by 16B-GC (Fig. 5). PW2 is characterized by a
312 significantly higher wet bulk density and p-wave velocity than other Upper Quaternary sediments in
313 the study region (Mattiessen et al., 2010; Schreck et al., 2018).

314

315 **5.3. Glaciogenic debris lobes on the AP slope**

316 The presence of debris lobes in the lower part of SSU 2 up-slope from core 16B (Fig. 2) is likely
317 related to glacial scouring on the AP crest. While debris flows can potentially originate from various
318 slope instability processes, the consistent occurrence of these lobes in the Arctic Ocean downslope from
319 continental margins and plateaus characterized by glacial erosion/deposition indicates their glaciogenic
320 origin. In particular, the CB features debris lobes on both the AP and Chukchi Plateau slopes (Niessen
321 et al., 2013; Dove et al., 2014 and reference therein), indicating glaciogenic inputs from both sides. The
322 mechanisms for debris flows could include sediment bulldozing on the tops by grounded ice and/or
323 rapid deposition of deglacial sediments, e.g., from glacial underflows (e.g., Powell, 1990; Batchelor
324 and Dowdeswell, 2015). The timing of debris lobe emplacement would thus correspond to glacial
325 advance or early deglaciation stages.

326 The SSW-NNE orientation and southward inclination of the youngest set of glacial lineations
327 on the AP top indicate that the eroding ice was sourced from the East Siberian margin (Niessen et al.,
328 2013). According to the age constraints developed for core 16B-GC and a correlative core 28B-GC
329 from the AP top (Fig. 5), this event occurred prior to the MIS 3 interstadial and was possibly related to
330 a major glaciation in northern Siberia dated to the time interval between ~70 and 50 ka (Svendsen et
331 al., 2004; Möller et al., 2015).

332 The upper seismostratigraphic unit SSU 1 bounded by the seafloor, and the W3 layer represents
333 deposition during the time interval from late MIS 3 to the Holocene (Fig. 6). The absence of glaciogenic
334 debris lobes within SSU 1 indicates that glacial erosion of the AP was unlikely during the LGM, as
335 suggested in previous studies (Niessen et al., 2013; Schreck et al., 2018).

336

337 **5.4. Glacier-induced depositional environments**

338 Based on the developed age model, sedimentary unit G2 (MIS 4 to early MIS 3) that is
339 characterized by laminated mud facies, has a relatively high sedimentation rate of ~6 cm/kyr as
340 compared to more bioturbated units G3 and G4 (Fig. 4, Table 2). Laminated structures of glaciogenic
341 sediments in the high-latitude oceans can be potentially formed under various depositional settings such
342 as permanent sea ice, turbid meltwater plumes, distal fine-grained turbidity currents, and contour
343 currents (Hesse et al., 1996; Darby et al., 1997; Kleiber et al., 2000; ÓCofaigh et al., 2003; Matthiessen
344 et al., 2010). However, contour currents are unlikely to be strong in a semi-enclosed Arctic deep-sea
345 basin, while sedimentation rates under perennial sea ice are too low to form a laminated sedimentary
346 sequence. Couplets of TLm/TLs and Hm facies similar to those observed in 16B-GC (Fig. 4) have been
347 interpreted in previous studies as deposition from underflow turbidity currents in combination with
348 rapid settling from fine-grained suspension plumes in the attenuation stage of the carrying current (Piper,
349 1978; Chough, 1984; Yoon et al., 1991). The occurrence of TLm/TLs facies within G2 and G3 suggests
350 that turbidities could be associated with the glaciogenic debris flows emanating from their front on a
351 relatively steep AP slope (Fig. 2B). The development of CLm facies may reflect deposition from turbid
352 meltwater plumes repeatedly discharged from ice-sheet termini (Hesse et al., 1996; Kleiber et al., 2000;
353 ÓCofaigh et al., 2003).

354 Glacial erosion on glaciated continental margins plays an important role in delivering large
355 amounts of sediments to the continental slope and the adjacent basins, and thus leading to the formation
356 of debris flows (Vorren et al., 1998; Kleiber et al., 2000; Dowdeswell and Elverhøi, 2002; Jakobsson et
357 al., 2008). Based on our seismostratigraphic and sediment core data, this scenario applies to the AP

358 during MIS 4, when large volumes of eroded sediment may have been transported as proglacial under-
359 and overflows into the adjacent deep basin. This rapid sediment deposition likely caused slope
360 instability and thus triggered debris flows. Suspended fine sediments could have been detached from
361 the slope and transported into the interior of the Arctic Ocean at the density boundaries between
362 different water masses with subsequent deposition. Prolonged glacial erosion could have also formed
363 repeatedly detached turbid layers, leading to the formation of **crudely laminated mud (CLm) facies** (Fig.
364 7A). As the grounded ice retreated, turbid meltwater underflow plumes were likely repeatedly
365 discharged from the grounding line, thereby depositing **CLm facies** (Hesse et al., 1996; ÓCofaigh et al.,
366 2003) (Fig. 7B). These glacier-induced processes could lead to the deposition of fine-grained, fully
367 laminated sediments with fairly high sedimentation rates (unit G2) during the MIS 4 deglaciation that
368 may have extended to early MIS 3.

369 Bioturbated sediments of B2 and the overlying W3 layer are interpreted to represent hemipelagic
370 depositional environments with drifting icebergs during a relatively warm period of MIS 3 (Fig. 7C).
371 In general, Mn-enriched, brown sediments are believed to reflect elevated sea levels and/or reduced
372 sea-ice conditions, under which sediment from the Siberian shelves could be transported to the central
373 Arctic basins (Jakobsson et al., 2000; Polyak et al., 2004, 2009; Stein et al., 2010; Löwemark et al.,
374 2014; Ye et al., 2019). Overall, sedimentary properties of G2 and overlying facies indicate depositional
375 environments affected by the advance and retreat of a marine-based ice sheet grounded on the AP top.

376 The absence of glaciogenic debris lobe within SSU 1 indicates that the AP has not encountered
377 glacial erosion during MIS 2, consistent with previous studies from the Arctic Ocean off the Siberian
378 margin (Niessen et al., 2013; Schreck et al., 2018) as well as terrestrial studies from adjacent islands
379 and the East Siberian mainland (Romanovskii et al., 2004; Gualtieri et al., 2005). Nevertheless, the
380 presence of CLm facies within unit G1, most of which is attributed to MIS 2 (Figs. 3, 4), reflects glacier-
381 induced depositional processes, such as the suspension settling of turbid meltwater plumes and detached
382 turbid layers (Figs 7D, E). This lithology indicates the influence of a limited glaciation in the study
383 region, although its location and distribution pattern (e.g., grounded ice vs. ice shelf) needs to be further

384 investigated. There is no evidence for the LGM glaciation at the East Siberian margin, but data from
385 the eastern Chukchi shelf margin show glaciogenic bedforms indicative of grounded ice, age-
386 constrained to MIS 2 (Polyak et al., 2007). These bedforms are restricted to water depths of less than
387 ~450 m, but we cannot exclude that this grounded ice extended over the Chukchi shelf to its western
388 margin bordering the Chukchi Basin.

389 The predominance of **the bioturbated sandy mud (Bsm)** facies in the uppermost unit B1 reflects
390 hemipelagic deposition with sea-ice and/or iceberg debris rafting during much of the Holocene (Fig.
391 7F). Intense bioturbation indicates a relatively elevated export of primary production to the seafloor,
392 and thus moderate sea-ice conditions, and/or enhanced oxygenation of surface sediments.

393

394 **6. Conclusions**

395 A combination of litho- and seismostratigraphy on the basinward slope of the Arliss Plateau
396 depicts a glacier-induced depositional history in front of the East Siberian continental margin since
397 estimated MIS 5c (~100 ka). The age constraints were obtained by correlation of the studied core
398 ARA02B/16B-GC with earlier developed stratigraphies (Adler et al., 2009; Schreck et al., 2018). Based
399 on this age model and the core-seismic correlation, deposition of the youngest glaciogenic debris lobes
400 on the slope, indicative of the last glacial erosion of the AP top, occurred within seismostratigraphic
401 unit SSU 2 during MIS 4 to early MIS 3. This event may be correlative to a major glaciation in northern
402 Siberia that has been constrained to the time interval between ~70 and 50 ka (Svendsen et al., 2004;
403 Möller et al., 2015). Laminated sedimentary facies and sedimentation rates as high as ~6 cm/kyr in the
404 respective core interval (lithological unit G2) reflect glacier-induced sediment deposition. This
405 enhanced sedimentation probably resulted from detached turbid layers, turbidity currents, and
406 meltwater discharge pulses during glaciation/deglaciation.

407 The absence of glaciogenic debris lobes within the upper seismostratigraphic unit SSU 1 (late
408 MIS 3 to 1) indicates that glacial erosion unlikely impacted the AP during the LGM, consistent with

409 previous inferences (Niessen et al., 2013; Schreck et al., 2018). Nevertheless, the presence of laminated
410 facies within the corresponding core interval G1 may indicate a limited glaciation at a nearby
411 continental margin. Further investigation by geophysical seafloor surveys verified by sediment core
412 records is needed to better understand the glacial history of the western Arctic Ocean.

413

414 **Acknowledgments**

415 We **want** to thank the captain and crew of RV Araon for excellent collaboration and support
416 during the 2nd Arctic expedition ARA02B in 2011. This research is mainly funded by a seed-type
417 research project (PE19350 to S.I. Nam) of Korea Polar Research Institute. LP contribution was partially
418 supported by the US National Science Foundation award ARC-1304755. We thank **an anonymous**
419 **reviewer and Matt O'Regan** for detailed comments that helped to improve the manuscript.

420

421 **References**

422 Adler, R.E., Polyak, L., Ortiz, J.D., Kaufman, D.S., Channell, J.E.T., Xuan, C., Grottoli, A.G., Sellén,
423 E., Crawford, K.A., 2009. Sediment record from the western Arctic Ocean with an improved Late
424 Quaternary age resolution: HOTRAX core HLY0503-8JPC, Mendeleev Ridge. *Glob. Planet.*
425 *Change* 68, 18-29.

426 Backman, J., Fornaciari, E., Rio, D., 2009. Biochronology and paleoceanography of late Pleistocene
427 and Holocene calcareous nannofossil abundances across the Arctic Basin. *Marine*
428 *Micropaleontology* 72, 86-98.

429 Batchelor, C.L., Dowdeswell, J.A., 2014. The physiography of High Arctic cross-shelf troughs. *Quat.*
430 *Sci. Rev.* 92, 68-96.

431 Batchelor, C.L., Dowdeswell, J.A., 2015. Ice-sheet grounding-zone wedges (GZWs) on high-latitude
432 continental margins. *Marine Geology*, 363: 65-92

433 Bazhenova, E., Fagel, N., Stein, R., 2017. North American origin of “pink–white” layers at the
434 Mendeleev Ridge (Arctic Ocean): New insights from lead and neodymium isotope composition of

435 detrital sediment component. *Mar. Geol.* 386, 44-55.

436 Bischof, J.F., Darby, D.A., 1997. Mid-to Late Pleistocene ice drift in the western Arctic Ocean:
437 evidence for a different circulation in the past. *Science* 277, 74-78.

438 Chough, S., 1984. Fine-grained turbidites and associated mass-flow deposits in the Ulleung (Tsushima)
439 Back-arc Basin, East Sea (Sea of Japan). *Geol. Soc. London Spec. Publ.* 15, 185-196.

440 Clark, D.L., Whitman, R.R., Morgan, K.A., Mackey, S.D., 1980. Stratigraphy and glacial-marine
441 sediments of the Amerasian Basin, central Arctic Ocean. Geological Society of America.

442 Cronin, T.M., Dwyer, G.S., Farmer, J., Bauch, H.A., Spielhagen, R.F., Jakobsson, M., Nilsson, J.,
443 Briggs Jr, W., Stepanova, A., 2012. Deep Arctic Ocean warming during the last glacial cycle. *Nature*
444 *Geoscience* 5, 631. Darby, D.A., Bischof, J.F., Jones, G.A., 1997. Radiocarbon chronology of
445 depositional regimes in the western Arctic Ocean. *Deep Sea Research Part II: Topical Studies in*
446 *Oceanography* 44, 1745-1757.

447 Dong, L., Liu, Y., Shi, X., Polyak, L., Huang, Y., Fang, X., Liu, J., Zou, J., Wang, K., Sun, F., Wang,
448 X., 2017. Sedimentary record from the Canada Basin, Arctic Ocean: implications for late to middle
449 Pleistocene glacial history. *Clim. Past* 13, 511-531.

450 Dove, D., Polyak, L., Coakley, B., 2014. Widespread, multi-source glacial erosion on the Chukchi
451 margin, Arctic Ocean. *Quat. Sci. Rev.* 92, 112-122.

452 Dowdeswell, J.A., Elverhøi, A., 2002. The timing of initiation of fast-flowing ice streams during a
453 glacial cycle inferred from glacial-marine sedimentation. *Mar. Geol.* 188, 3-14.

454 England, J.H., Furze, M.F., Doupe, J.P., 2009. Revision of the NW Laurentide Ice Sheet: implications
455 for paleoclimate, the northeast extremity of Beringia, and Arctic Ocean sedimentation. *Quat. Sci.*
456 *Rev.* 28, 1573-1596.

457 Grobe, H., 1987. A simple method for the determination of ice-rafted debris in sediment cores.
458 *Polarforschung* 57, 123-126.

459 Gualtieri, L., Vartanyan, S., Brigham-Grette, J., Anderson, P., 2005. Evidence for an ice-free Wrangel
460 Island, northeast Siberia during the Last Glacial Maximum. *Boreas* 34, 264-273.

461 Hanslik, D., Jakobsson, M., Backman, J., Björck, S., Sellén, E., O'Regan, M., Fornaciari, E., Skog, G.,

462 2010. Pleistocene Arctic Ocean sea ice and deep water isolation times. *Quat. Sci. Rev* 29, 3430-
463 3441.

464 Hesse, R., Klauke, I., Ryan, W.B., Edwards, M.B., Piper, D.J.W., 1996. Imaging Laurentide Ice Sheet
465 Drainage into the Deep Sea: Impact on Sediments and Bottom Water. *Oceanographic Literature*
466 *Review* 4.

467 Jakobsson, M., Andreassen, K., Bjarnadóttir, L.R., Dove, D., Dowdeswell, J.A., England, J.H., Funder,
468 S., Hogan, K., Ingólfsson, Ó., Jennings, A., Krog Larsen, N., Kirchner, N., Landvik, J.Y., Mayer,
469 L., Mikkelsen, N., Möller, P., Niessen, F., Nilsson, J., O'Regan, M., Polyak, L., Nørgaard-Pedersen,
470 N., Stein, R., 2014. Arctic Ocean glacial history. *Quat. Sci. Rev.* 92, 40-67.

471 Jakobsson, M., Grantz, A., Kristoffersen, Y., Macnab, R., 2003. Physiographic provinces of the Arctic
472 Ocean seafloor. *Geol. Soc. Am. Bull.* 115.

473 Jakobsson, M., Løvlie, R., Al-Hanbali, H., Arnold, E., Backman, J., Mörth, M., 2000. Manganese and
474 color cycles in Arctic Ocean sediments constrain Pleistocene chronology. *Geology* 28, 23-26.

475 Jakobsson, M., Løvlie, R., Arnold, E., Backman, J., Polyak, L., Knutsen, J.-O., Musatov, E., 2001.
476 Pleistocene stratigraphy and paleoenvironmental variation from Lomonosov Ridge sediments,
477 central Arctic Ocean. *Glob. Planet. Change* 31, 1-22.

478 Jakobsson, M., Nilsson, J., Anderson, L., Backman, J., Björk, G., Cronin, T.M., Kirchner, N.,
479 Koshurnikov, A., Mayer, L., Noormets, R., O'Regan, M., Stranne, C., Ananiev, R., Barrientos
480 Macho, N., Cherniykh, D., Coxall, H., Eriksson, B., Flodén, T., Gemery, L., Gustafsson, Ö., Jerram,
481 K., Johansson, C., Khortov, A., Mohammad, R., Semiletov, I., 2016. Evidence for an ice shelf
482 covering the central Arctic Ocean during the penultimate glaciation. *Nature Communications* 7,
483 10365.

484 Jakobsson, M., Polyak, L., Edwards, M., Kleman, J., Coakley, B., 2008. Glacial geomorphology of the
485 Central Arctic Ocean: the Chukchi Borderland and the Lomonosov Ridge. *Earth Surf. Proc. Land.*
486 33, 526-545.

487 **Jokat, W., 2008. The expedition of the research vessel "Polarstern" to the Arctic in 2008 (ARK-XXIII/3).**

488 Kaufman, D.S., Polyak, L., Adler, R., Channell, J.E., Xuan, C., 2008. Dating late Quaternary planktonic

489 foraminifer *Neogloboquadrina pachyderma* from the Arctic Ocean using amino acid racemization.
490 *Paleoceanography* 23.

491 Kleiber, H., Knies, J., Niessen, F., 2000. The Late Weichselian glaciation of the Franz Victoria Trough,
492 northern Barents Sea: ice sheet extent and timing. *Mar. Geol.* 168, 25-44.

493 Löwemark, L., März, C., O'Regan, M., Gyllencreutz, R., 2014. Arctic Ocean Mn-stratigraphy: genesis,
494 synthesis and inter-basin correlation. *Quat. Sci. Rev.* 92, 97-111.

495 Löwemark, L., O'Regan, M., Hanebuth, T., Jakobsson, M., 2012. Late Quaternary spatial and temporal
496 variability in Arctic deep-sea bioturbation and its relation to Mn cycles. *Paleogeogr. Paleoclimatol.*
497 *Paleoecol.* 365, 192-208.

498 März, C., Stratmann, A., Matthiessen, J., Meinhardt, A.K., Eckert, S., Schnetger, B., Vogt, C., Stein,
499 R., Brumsack, H.J., 2011. Manganese-rich brown layers in Arctic Ocean sediments: Composition,
500 formation mechanisms, and diagenetic overprint. *Geochimica et Cosmochimica Acta* 75, 7668-7687.

501 Matthiessen, J., Niessen, F., Stein, R., Naafs, B.D.A., 2010. Pleistocene glacial marine sedimentary
502 environments at the eastern Mendeleev Ridge, Arctic Ocean. *Polarforschung* 79, 123-137.

503 Möller, P., Alexanderson, H., Funder, S., Hjort, C., 2015. The Taimyr Peninsula and the Severnaya
504 Zemlya archipelago, Arctic Russia: a synthesis of glacial history and palaeo-environmental change
505 during the Last Glacial cycle (MIS 5e–2). *Quat. Sci. Rev.* 107, 149-181.

506 Niessen, F., Hong, J.K., Hegewald, A., Matthiessen, J., Stein, R., Kim, H., Kim, S., Jensen, L., Jokat,
507 W., Nam, S.-I., 2013. Repeated Pleistocene glaciation of the East Siberian continental margin.
508 *Nature Geoscience* 6, 842.

509 Nørgaard-Pedersen, N., Spielhagen, R.F., Thiede, J., Kassens, H., 1998. Central Arctic surface ocean
510 environment during the past 80,000 years. *Paleoceanography* 13, 193-204.

511 O'Regan, M., Backman, J., Barrientos, N., Cronin, T.M., Gemery, L., Kirchner, N., Mayer, L.A.,
512 Nilsson, J., Noormets, R., Pearce, C., 2017. The De Long Trough: a newly discovered glacial trough
513 on the East Siberian continental margin. *Clim. Past* 13, 1269.

514 ÓCofaigh, C., Taylor, J., Dowdeswell, J.A., Pudsey, C.J., 2003. Palaeo-ice streams, trough mouth fans
515 and high-latitude continental slope sedimentation. *Boreas* 32, 37-55.

516 Phillips, L. R., Grantz, A., 1997. Quaternary history of sea ice and paleoclimate in the Amerasia basin,
517 Arctic Ocean, as recorded in the cyclical strata of Northwind Ridge. *Geol. Soc. Am. Bull.* 109,
518 1101-1115.

519 Piper, D.W., 1978. Turbidite muds and silts on deepsea fans and abyssal plains. In Stanley, D.J. and
520 Kelling, G. (eds.), *Sedimentation in submarine canyons, fans, and trenches*, Hutchinson and Ross
521 Stroudsburg, 163-176.

522 Poirier, R.K., Cronin, T.M., Briggs Jr, W.M., Lockwood, R., 2012. Central Arctic paleoceanography
523 for the last 50 kyr based on ostracode faunal assemblages. *Marine Micropaleontology* 88, 65-76.

524 Polyak, L., Bischof, J., Ortiz, J.D., Darby, D.A., Channell, J.E.T., Xuan, C., Kaufman, D.S., Løvlie, R.,
525 Schneider, D.A., Eberl, D.D., Adler, R.E., Council, E.A., 2009. Late Quaternary stratigraphy and
526 sedimentation patterns in the western Arctic Ocean. *Glob. Planet. Change* 68, 5-17.

527 Polyak, L., Curry, W.B., Darby, D.A., Bischof, J., Cronin, T.M., 2004. Contrasting glacial/interglacial
528 regimes in the western Arctic Ocean as exemplified by a sedimentary record from the Mendeleev
529 Ridge. *Paleogeogr. Paleoclimatol. Paleoecol.* 203, 73-93.

530 Polyak, L., Darby, D.A., Bischof, J.F., Jakobsson, M., 2007. Stratigraphic constraints on late
531 Pleistocene glacial erosion and deglaciation of the Chukchi margin, Arctic Ocean. *Quat. Res.* 67,
532 234-245.

533 Powell, R.D., 1990, Glacimarine processes at grounding-line fans and their growth to ice-contact deltas,
534 in Dowdeswell, J.A., and Scourse, J.D., eds., *Glacimarine Environments: Processes and Sediments:*
535 *Geological Society of London Special Publication* 53, p. 53–73.

536 Romanovskii, N., Hubberten, H.-W., Gavrillov, A., Tumskey, V., Kholodov, A., 2004. Permafrost of
537 the east Siberian Arctic shelf and coastal lowlands. *Quat. Sci. Rev.* 23, 1359-1369.

538 Schreck, M., Nam, S.-I., Polyak, L., Vogt, C., Kong, G.S., Stein, R., Matthiessen, J., Niessen, F., 2018.
539 Improved Pleistocene sediment stratigraphy and paleoenvironmental implications for the western
540 Arctic Ocean off the East Siberian and Chukchi margins. *arktos* 4.

541 Spielhagen, R.F., Baumann, K.-H., Erlenkeuser, H., Nowaczyk, N.R., Nørgaard-Pedersen, N., Vogt,
542 C., Weiel, D., 2004. Arctic Ocean deep-sea record of northern Eurasian ice sheet history. *Quat. Sci.*

543 Rev. 23, 1455-1483.

544 Stein, R., Matthiessen, J., Niessen, F., Krylov, A., Nam, S.-I., Bazhenova, E., 2010. Towards a better
545 (litho-) stratigraphy and reconstruction of Quaternary paleoenvironment in the Amerasian Basin
546 (Arctic Ocean). *Polarforschung* 79, 97-121.

547 Stokes, C., Margold, M., Clark, C., Tarasov, L., 2016. Ice stream activity scaled to ice sheet volume
548 during Laurentide Ice Sheet deglaciation. *Nature* 530, 322.

549 Svendsen, J., 2004. Late Quaternary ice sheet history of northern Eurasia. *Quat. Sci. Rev.* 23, 1229-
550 1271. Thierstein, H., Geitzenauer, K., Molino, B., Shackleton, N., 1977. Global synchronicity of late
551 Quaternary coccolith datum levels Validation by oxygen isotopes. *Geology* 5, 400-404.

552 Vorren, T.O., Laberg, J.S., F., B., Dowdeswell, J.A., N.H., K., J., M., J., R., Werner, F., 1998. The
553 Norwegian-Greenland Sea Continental Margins: Morphology and Late Quaternary Sedimentary
554 Processes and Environment. *Quat. Sci. Rev.* 17, 273-302.

555 Wang, R., Polyak, L., Xiao, W., Wu, L., Zhang, T., Sun, Y., Xu, X., 2018. Late-Middle Quaternary
556 lithostratigraphy and sedimentation patterns on the Alpha Ridge, central Arctic Ocean: Implications
557 for Arctic climate variability on orbital time scales. *Quat. Sci. Rev.* 181, 93-108.

558 Wang, R., Xiao, W., März, C., Li, Q., 2013. Late Quaternary paleoenvironmental changes revealed by
559 multi-proxy records from the Chukchi Abyssal Plain, western Arctic Ocean. *Glob. Planet. Change*
560 108, 100-118.

561 Ye, L., März, C., Polyak, L., Yu, X., Zhang, W., 2019. Dynamics of manganese and cerium enrichments
562 in Arctic Ocean sediments: a case study from the Alpha Ridge. *Frontiers in Earth Science* 6.

563 Yoon, S., Chough, S., Thiede, J., Werner, F., 1991. Late Pleistocene sedimentation on the Norwegian
564 continental slope between 67 and 71 N. *Mar. Geol.* 99, 187-207.

565

566

567

568

569

570 **Figure and Table captions**

571 **Figure 1** (A) Index physiographic map of the study area showing the location of cores ARA02B/16B-
572 GC (this study), ARA03B/28B-GC (Schreck et al., 2018) and HLY0503-8JPC (Adler et al., 2009). MR,
573 Mendeleev Ridge; AP, Arliss Plateau; CB, Chukchi Basin; CP, Chukchi Plateau; NR, Northwind Ridge.
574 Solid line tracks sub-bottom profiler data. Bathymetric contour interval is 250 m. (B) Broader
575 physiographic/paleogeographic context with inferred ice-sheet maxima shown by semi-transparent
576 white fill (Svendsen et al., 2004; Niessen et al., 2013; Stokes et al., 2016). (C) Multibeam bathymetry
577 of the Arliss Plateau showing several generations of Mega-Scale Glacial Lineations. Bathymetric
578 contour interval is 100 m.

579 **Figure 2** Sub-bottom profiler from Arliss Plateau to Chukchi Basin across the site of core
580 ARA02B/16B-GC (red vertical bar in panel B). Seismostratigraphic units SSU 1 and 2 are bounded by
581 distinct reflectors R1 to 3. The uppermost glaciogenic debris lobes on the slope are correlated with the
582 lower part of SSU 2. Black box shows the position of Fig. 6.

583 **Figure 3** Down-core distribution of sediment lightness (L^*), Mn/Al and Ca/Al ratios, IRD numbers,
584 and grain size in core ARA02B/16B-GC. Top 10 cm are estimated to be missing due to overpenetration;
585 XRF data for this interval (blue-colored solid lines) are spliced from the box core 16B-BC. High Mn/Al
586 and Ca/Al ratios in surficial sediment may be partially due to high water content (Thallinghii et al.,
587 2007). Lithostratigraphic indices are shown in Fig. 3.

588 **Figure 4** Split-core photos, X-radiograph images, and sedimentary facies (see Table 1 for details).
589 Indices for lithological units (B1-B5 and G1-G4) and the detrital carbonate layer W3 are shown on the
590 core photo.

591 **Figure 5** Lithostratigraphic correlation of core ARA02B/16B-GC with ARA03B/28B-GC (Schreck et
592 al., 2018) and HLY0503-8JPC (Adler et al., 2009) based on sediment color and variations of Mn/Al
593 and Ca/Al. The tops of major brown units (B2-B5) are correlated by dotted lines; the bottom of core

594 ARA03B/28B-GC is projected onto ARA02B/16B-GC by the dashed line. Estimated Marine Isotope
595 Stages and radiocarbon/AAR ages (Adler et al., 2009) are shown next to core HLY0503-8JPC.

596 **Figure 6** Correlation of the subbottom data with core ARA02B/16B-GC. Surficial reflector R1 is the
597 seafloor. Strong reflectors R2 and R3 correspond to prominent lithological changes at the boundaries
598 of fine-grained sediments and IRD-rich layers W3 and PW2. Estimated Marine Isotope Stages are
599 shown on the right.

600 **Figure 7** Schematic model of sedimentary processes on the Arliss Plateau and adjacent Chukchi Basin
601 during major depositional regimes from the MIS 4 glaciation to the Holocene.

602

603 **Table 1** Summary of sedimentary facies in core ARA02B/16B-GC. Black arrows indicate the intervals
604 of TLM, TLs, and Hm facies. See Fig. 4 for the stratigraphic distribution of sedimentary facies.

605 **Table 2** Estimated duration and sedimentation rates of lithostratigraphic units in core ARA02B/16B-
606 GC based on the age model developed from lithostratigraphic correlations (Fig. 5).

1 **Late Quaternary depositional and glacial history of the Arliss Plateau off the East**
2 **Siberian margin in the western Arctic Ocean**

3
4 Young Jin Joe^{1,2}, Leonid Polyak³, Michael Schreck^{1,4}, Frank Niessen⁵, Seok Hoon Yoon²,
5 Gee Soo Kong⁶, Seung-Il Nam^{1,*}
6

7 ¹Division of Polar Paleoenvironment, Korea Polar Research Institute, 21990 Incheon, Republic of Korea

8 ²Department of Earth and Marine Sciences, Jeju National University, 63243 Jeju, Republic of Korea

9 ³Byrd Polar and Climate Research Center, The Ohio State University, 1090 Carmack Road, Columbus, OH,
10 43210, USA.

11 ⁴Department of Geosciences, UiT-The Arctic University of Norway, N-9037 Tromsø, Norway

12 ⁵Alfred Wegener Institute (AWI) Helmholtz Centre for Polar and Marine Research, D- 27568 Bremerhaven,
13 Germany

14 ⁶Petroleum and Marine Division, Korea Institute of Geoscience and Mineral Resources, 34132 Daejeon,
15 Republic of Korea
16
17
18
19
20
21
22

23 *Corresponding Author: Seung-Il Nam (sinam@kopri.re.kr)
24

25 Keywords: Arctic Ocean sediments, Late Quaternary, glacial history, sediment facies, seismostratigraphy
26

27 **Abstract** Sedimentary stratigraphy and facies analysis along with seismostratigraphic and
28 multibeam bathymetry data are used to reconstruct the last glacial impact on the Arliss Plateau (AP)
29 and attendant sedimentation in the adjacent Chukchi Basin (CB) in the western Arctic Ocean off the
30 East Siberian margin. Sediment core ARA02B/16B-GC from the AP lower slope captures glacier-
31 related depositional history during the last estimated ca. 100 ka (Marine Isotope Stage (MIS) 1 to 5c)
32 based on regional lithostratigraphic correlation. The sedimentary record shows distinguishable
33 interglacial (interstadial) and glacial (stadial) patterns. The identified sedimentary facies reflect several
34 modes of glaciogenic deposition by drifting icebergs, suspension settling from turbid meltwater plumes
35 and/or detached underflows, and turbidity currents. Based on strong seismic reflectors related to
36 lithological boundaries, a downslope subbottom profile from AP to CB is divided into
37 seismostratigraphic units (SSU) 1 and 2 corresponding in the core record to MIS 1-3 and MIS 3-5c,
38 respectively. An acoustically transparent lens within SSU 2 correlates on the upper slope to debris lobes
39 downslope from the AP top covered by megascale glacial lineations. This geomorphic/sedimentary
40 pattern indicates a glacial erosional impact on the AP and proglacial deposition of eroded sediments on
41 the slope and in the basin. Based on the developed sediment stratigraphy and facies analysis, the last
42 debris lobe horizon was deposited in glacial/deglacial environments during late MIS 4 to early MIS 3.
43 The absence of similar glaciogenic debris lobes within SSU 1 indicates no direct glacial impact on the
44 AP during the Last Glacial Maximum (MIS 2). These results suggest that the last glacial erosion of the
45 AP occurred during or immediately after MIS 4, possibly related to major glaciation in northern Siberia
46 at ~50-70 ka.

47 **1. Introduction**

48 Over last two decades, multiple geophysical investigations along with sedimentary records
49 revealed that the Arctic East Siberian and Chukchi continental margins have been repeatedly glaciated
50 during the Pleistocene (Jakobsson et al., 2008, 2014; Polyak et al., 2007; Niessen et al., 2013; Dove et
51 al., 2014; O'Regan et al., 2017). In particular, streamlined glacial lineations and related diamicton
52 deposits identified by swath seafloor and subbottom profiling on the East Siberian margin, including
53 the adjacent part of the Mendeleev Ridge known as the Arliss Plateau (AP) (Fig. 1C), indicate the
54 repeated development of up to 1 km-thick marine ice sheets/ice shelves (Niessen et al., 2013). However,
55 the age framework for these glacial events, and thus, their relation to a broader paleoclimatic context,
56 is not well understood. Recently, Schreck et al. (2018) provided lithostratigraphic insight on glacial
57 impacts on the East Siberian margin in the Late Pleistocene, concluding that the last major regional ice
58 grounding occurred during MIS 4 to 3 (60-70 ka). This conclusion differs from the notion that this event
59 was coeval with the deepest glacial erosion on the Lomonosov Ridge in the central Arctic Ocean
60 (Jakobsson et al., 2016; O'Regan et al., 2017), which has been constrained to MIS 6 (Jakobsson et al.,
61 2001).

62 To better constrain the timing of ice grounding events and their spatial pattern, it is important to
63 link the geophysical records and sediment core stratigraphy. This task requires analyzing representative
64 sedimentary records accompanied by sub-bottom seismic profiles and detailed multibeam bathymetry
65 from the areas affected by glaciations. However, most areas of continental margins, as well as
66 bathymetric highs on the oceanic ridges and plateaus impacted by glacial erosion or iceberg turbation,
67 are unsuitable for recovering well preserved, stratigraphically coherent records (Polyak et al., 2007;
68 Jakobsson et al., 2008; Dove et al., 2014). In comparison, the adjacent slopes and basins may hold more
69 expanded, better-preserved stratigraphies, provided their depositional context, which is sufficiently
70 constrained by geophysical data. In particular, the slope of the AP and the adjacent Chukchi Basin (CB)
71 was chosen for this study as a relatively well surveyed area of deposition for glaciogenic material
72 originating from the East Siberian continental margin (Niessen et al., 2013; Jakobsson et al., 2014;
73 Schreck et al., 2018). We are using a sediment core collected on a CHIRP sub-bottom profile (SBP)
74 from the AP top to the CB (Fig. 1) to reconstruct the depositional history of the East Siberian margin
75 during and since the last glacial grounding event.

76

77 **2. Regional setting**

78 **2.1. Seafloor morphology and sedimentary cover**

79 The CB is bounded by the Mendeleev Ridge/AP and the Chukchi Plateau and shelf and is
80 connected to the north with the Canada Basin (Fig. 1). The CB covers ~43,000 km² (Jakobsson et al.,
81 2003) and has a relatively flat and smooth seafloor ranging from 1,800 m to 2,300 m water depth and
82 comprised of well-stratified deposits (Dove et al., 2014). The tops of both the Arliss and the Chukchi
83 plateaus are covered by streamlined morphological features interpreted as megascale glacial lineations
84 (MSGSL), complicated in some areas with transverse ridges (Niessen et al., 2013; Dove et al., 2014;
85 Jakobsson et al., 2014, 2016). The outer parts of the East Siberian and Chukchi margins at water depths
86 to 700 m feature extensive till wedges and recessional moraines related to repeated glacial advances
87 and retreats (Niessen et al., 2013; Dove et al., 2014; Jakobsson et al., 2014). Further downslope these
88 margins as well as adjacent borderlands, including the AP, hold large, lens-shaped debris lobes (Fig. 2),
89 similar to seismostratigraphic features observed in the glacial trough mouth fans in front of large ice
90 streams (Batchelor and Dowdeswell, 2014; Jakobsson et al., 2014; O'Regan et al., 2017).

91

92 **2.2. Sediment stratigraphy in the western Arctic Ocean**

93 The Quaternary western Arctic sediments are generally characterized by the cyclical pattern of
94 dark brownish and olive/greyish units (Phillips and Grantz, 1997; Polyak et al., 2004, 2009; Adler et
95 al., 2009; Stein et al., 2010; Schreck et al., 2018). This color contrast was shown to be controlled by the
96 content of manganese (Mn) oxy(hydr)oxides, with higher values in brown units attributed to Mn inputs
97 from the continental margins at higher sea levels during interglacial/major interstadial periods
98 (Jakobsson et al., 2000; Polyak et al., 2004, 2009; März et al., 2011; Löwemark et al., 2014; Ye et al.,
99 2019). While Mn-enriched intervals can be affected by diagenetic remobilization and redistribution of
100 this redox-sensitive element, their stratigraphic pattern is consistent throughout the central Arctic Ocean

101 (März et al., 2011; Löwemark et al., 2014; Schreck et al., 2018). Their correlation is corroborated in
102 multiple cores by the distribution of other lithostratigraphic parameters, such as sediment density, ice-
103 rafted debris (IRD), and biogenic proxies. The brown, Mn-enriched units (layers), interpreted as
104 interglacial/major interstadial sedimentary intervals, are typically characterized also by low to moderate
105 amounts of coarse IRD, intense bioturbation, and relatively abundant microfossils (Polyak et al., 2004,
106 2009; Adler et al., 2009; Stein et al., 2010; Löwemark et al., 2012). In comparison, olive/greyish, Mn-
107 depleted units, related to glacial periods, are composed of fossil-poor sediments with strongly variable
108 IRD amounts (Polyak et al., 2004, 2009; Adler et al., 2009; Stein et al., 2010). Fine-grained and IRD-
109 rich lithological types of grey sediments have been attributed to glacial maxima and deglacial
110 depositional environments, respectively. At sites proximal to glaciated areas, deglacial sediments may
111 have expanded thicknesses indicative of high depositional rates (Polyak et al., 2007; Wang et al., 2013;
112 Schreck et al., 2018). Some of the IRD peaks have characteristic sediment compositions used as
113 provenance indicators. In particular, detrital carbonates (mostly dolomites) are related to the Paleozoic
114 platform of the Canadian Arctic eroded by the Laurentide Ice Sheet (LIS) (Bischof and Darby, 1997;
115 England et al., 2009; Polyak et al., 2009; Stein et al., 2010; Bazhenova et al., 2017; Dong et al., 2017).
116 Peaks of this material forming characteristic pinkish-white (PW) layers in sediment cores (Clark et al.,
117 1980) can be used to track the distribution of icebergs in the Arctic Ocean during the LIS collapse events.

118

119 **3. Material and methods**

120 **3.1. Material**

121 We use a 378-cm-long, 12-cm in diameter gravity sediment core ARA02B/16B-GC (hereafter
122 16B-GC) and high frequency (2.5-6.5 kHz) subbottom CHIRP profiler data collected on the AP slope
123 (Fig. 1) during the 2nd RV *Araon* Arctic Expedition (ARA02B) in 2011. Multibeam bathymetry
124 mapping of the AP top (Fig. 1C) was subsequently conducted in 2012 (ARA03B). The 16B-GC coring
125 site (76° 24' N, 175° 58' W, 1841 meter water depth (mwd)) was selected based on the AWI Parasound
126 data acquired previously on the 2008 RV *Polarstern* Arctic expedition ARK-24/3 (Jokat, 2008). The

127 site is located ~1 km downslope from the foot of glaciogenic debris lobes and features relatively flat
128 and smooth seafloor with acoustically well stratified subbottom reflectors (Fig. 2). A 38-cm-long box
129 core 16B-BC was taken at the same site to recover the surficial sediment. Based on the comparison with
130 16B-BC, about 10 cm of top sediment is lost in 16B-GC, including the surficial brown lithological unit
131 B1, which was spliced for a composite record of 16B-BC (Figs. 3, 4).

132

133 **3.2. Methods**

134 After a visual description of the split core, its line-scan images and elemental geochemistry were
135 acquired with AVAATECH XRF-core scanner at Korea Institute of Geoscience and Mineral Resources
136 (KIGAM). Line-scanning was conducted using a Jai CV L107 camera with red-green-blue (RGB)
137 channels. L* (lightness) and a* (red-green color space) data were used for correlation with previously
138 published sediment records (Schreck et al. 2018). Sediment elemental composition was measured at 5-
139 mm intervals using X-ray fluorescence (XRF) AVAATECH scanner settings reported in Schreck et al.
140 (2018). Mn and calcium (Ca) XRF data used in lithostratigraphic correlation were normalized to
141 aluminum (Al) to eliminate the potential dilution effect of background sedimentation (e.g., März et al.,
142 2011). We note, however, that Mn and Ca variations in Arctic sediments are largely independent of the
143 background lithogenic elements as shown in prior studies (e.g., Löwemark et al., 2014; Dong et al.,
144 2017)

145 X-radiographs were performed for detailed sediment structure on 1 x 10 x 30 cm slabs. X-ray
146 images were taken with SOFTEX m-100w digital x-ray scanner (EZ-320) and instantly processed using
147 iX-Pect X-Ray imaging software. Darker objects in X-radiographs presented in this study display dense
148 material, such as lithic fragments. Coarse debris >2 mm in diameter was counted at every 1 cm,
149 according to Grobe (1987). Samples for sediment texture were taken at 10 cm intervals and treated with
150 35% H₂O₂ to decompose organic matter. Sand-sized and coarser grains were separated by wet sieving
151 at 63 µm and dry sieving at 2 mm standard sieves. The grain size of <63-µm sediment was measured
152 with a Micromeritics Sedigraph 5000D.

153 The multibeam bathymetric survey was performed using a hull-mounted EM122 echosounder.
154 Acquired bathymetric data were processed onboard using a specialized software CARIS. Sub-bottom
155 seismic-reflection data were acquired with the CHIRP SBP-120 profiler with the vertical resolution on
156 the 10 cm scale in acoustically stratified sediments. The SBP data were logged in the TOPAS raw
157 format, which was converted to an SEG-Y format and allowed for post-processing with standard
158 software packages. The estimated sound velocity of 1500 m/s was used to convert the signal travel time
159 into sediment depth for comparison with core lithostratigraphy.

160

161 **4. Results**

162 **4.1. Lithostratigraphy**

163 Core 16B is composed of sandy to fine-grained mud displaying a general cyclic depositional
164 pattern characterized by an alternation of brown to dark brown and yellow to olive greyish sedimentary
165 units (Figs. 3, 4). The concentration of coarse IRD (>2 mm) increases at lithological boundaries and
166 within some brown units, whereas IRD within yellow to olive greyish units is typically rare.

167 A total of five Mn-rich brown units, B1 to B5, are identified in the recovered stratigraphy based
168 on sediment color, and Mn/Al ratio (Fig. 3) along with sedimentary structure and texture (Fig. 4),
169 including the upper unit B1 spliced from the box core 16B-BC. The brown units show a characteristic
170 low-L* (darker) and high-a* (more reddish) color pattern with a relatively symmetrical distribution
171 across each unit (Fig. 3). High Mn/Al ratios in surficial sediments may be partially due to high water
172 content (Thallingii et al., 2007), but that does not affect the stratigraphic distribution of Mn values,
173 which are high in unit B1. The brown units mostly consist of slightly sandy mud with scattered IRD
174 and have relatively sharp upper boundary and uneven, bioturbated (mottled) lower boundary (Fig. 4).
175 Yellowish to olive-grey units are generally thicker than brown units and are mostly composed of fine-
176 grained mud without coarse IRD. In particular, the second grey unit between B2 and B3 is the thickest
177 interval recovered (~150 cm) with a consistent lithology. Two PW carbonate layers, consisting of

178 sandy-gravelly mud and expressed as relatively solid lenses and adjacent scattered speckles, are
179 identified above B2 and at the base of B3, corresponding to prominent Ca/Al peaks (Figs. 3, 4).

180

181 **4.2. Sediment facies**

182 Sediment of core 16B was classified into five major facies based on sedimentary structure,
183 texture, and color (Fig. 4, Table 1): bioturbated sandy mud (Bsm), bioturbated mud (Bm), crudely
184 laminated or layered mud (CLm), thinly laminated mud/muddy sand (TLm/TLs), and homogeneous
185 mud (Hm).

186 Bioturbated sandy mud (Bsm) is mostly identified in brown units and PW carbonaceous layers
187 and is characterized by strong bioturbation overprinting primary sedimentary structures, sharp upper-
188 and uneven, mottled lower-boundaries (Fig. 4). This facies mainly consists of very poorly sorted (2 – 4
189 Φ) sandy mud with coarse particles randomly scattered within the fine matrix (Fig. 3). In comparison
190 with the brown units, Bsm in the PW layers contains higher sand content, up to 22% (Fig. 3), and more
191 coarse particles.

192 Bioturbated mud (Bm) generally occurs at the transitions between brown and olive-grey units
193 and is characteristic for the olive-grey units underlying B1, where Bm is interbedded with the crudely
194 laminated or layered mud facies (CLm), and below B3 (Fig. 4). Similar to Bsm, the Bm facies also has
195 a mottled structure but is composed of more fine-grained muds with gradual facies boundaries. The
196 sediment sorting index in this facies (1 – 1.5 Φ) is lower than in Bsm due to a lack of coarse particles
197 (Figs. 3, 4).

198 Crudely laminated or layered mud (CLm) is characterized by the alternation of planar to sub-
199 parallel silt- and clay-rich laminae or layers with weak bioturbation (Fig. 4). Individual laminae are
200 generally difficult to discern. Clayey laminae/layers are mostly thicker (4 – 12 mm) than their silt-rich
201 counterparts (1 – 3 mm). Vertical changes in lamina thickness and composition appear to be random,
202 and the sediment is overall weakly sorted (1 – 1.5 Φ). Facies CLm is predominant within the second

203 olive-grey unit bounded by B2 and B3 and is also interbedded with the Bm facies in the first olive-grey
204 unit.

205 Thinly laminated mud/muddy sand facies (TLm/TLs) can be subdivided into silt-rich mud (TLm)
206 and muddy sand (TLs). This distinct facies has a laterally continuous lamination (a few millimeters
207 thick), typically identified as couplets with overlying homogeneous mud facies Hm (Fig 4). TLm/TLs
208 laminae show sharp lower and gradational upper boundaries, and relatively regular thicknesses (Fig. 3).
209 TLm/TLs facies occur episodically in the second and third olive-grey intervals, between B2 – B3 and
210 B3 – B4, respectively (Figs. 3, 4).

211 Homogeneous mud facies (Hm) consists of fine-grained muddy sediment characterized by an
212 overall absence of primary structures, bioturbation, or any grading. This facies is mostly interbedded
213 with the thinly laminated facies TLm/TLs on millimeter scales as couplets. Independently occurring
214 Hm facies (3 cm thick) is identified only in the upper part of the third olive-grey interval below B3 (Fig.
215 4).

216

217 **4.3. Geomorphology and seismostratigraphy of the AP basinward slope**

218 The seafloor of the AP top shows several sets of streamlined morphological features (Fig. 1C)
219 interpreted in prior studies as megascale glacial lineations (Niessen et al., 2013; Jakobsson et al., 2016).
220 The youngest set of lineations of SSW-NNE orientation is traced to water depths of ~950 m in the
221 southern part of AP, compared to somewhat shallower depths of 850 m in the northern part. The lineated
222 surface is covered by ~3-m thick, acoustically stratified sediment (Niessen et al., 2013).

223 The subbottom data from the basin-ward middle to the lower slope of the AP (~1600-1800 mwd)
224 show stacked series of debris lobes of ~10-20 km long and up to 25 m thick (Fig. 2A). The debris
225 deposits are covered by acoustically stratified sediments (Figs. 2B, C). Three distinct acoustic reflectors
226 (R1 – R3) were identified by lateral continuity and strong reflectivity. The reflectors divide the upper
227 part of the sediment cover into two major seismostratigraphic units, SSU 1 and 2.

228 The surficial unit SSU 1 bounded by reflectors R1 (seafloor) and R2 is laterally continuous and
229 has bedding parallel to R2 (Figs 2B and C). SSU 1 is characterized by transparent to slightly fuzzy sub-
230 bottom echoes, with a laterally discontinuous, weak reflector also recognized within this unit (Fig. 2B).
231 SSU 1 thins out from the core 16B site towards the steep middle slope (Figs. 2B and C) and is
232 indistinguishable further up-slope near the AP top.

233 As seen on records from the basin and lower slope (Fig. 2B), the underlying unit SSU 2, bounded
234 by R2 and R3, is generally characterized by parallel lamination with variable amplitudes and transparent
235 acoustic signature in the middle part of the unit. Further up-slope, two coeval debris lobes are
236 recognized in the lower part of SSU 2, covered by acoustically stratified sediment comprised of the
237 remaining part of SSU 2 and overlying SSU 1 (Figs. 2B, C). Two thin reflectors with low to moderate
238 reflectivity are identified in the lowermost part of SSU 2 in the basin, but cannot be found near the
239 debris lobes on the upper slope (Fig. 2B).

240

241 **5. Discussion**

242 **5.1. Age model**

243 As core 16B-GC lacks calcareous material for ^{14}C dating, its age model is constrained by
244 lithostratigraphic correlation with the earlier investigated core ARA03B/28B-GC from the AP top
245 (Schreck et al., 2018) and core HLY0503-8JPC from the foot of the Mendeleev Ridge ~350 km north
246 (Adler et al., 2009). The latter core record has the best regional age control constrained by multiple ^{14}C
247 datings in the upper part of the stratigraphy (MIS 1 to 3, units B1-B3), ^{14}C -calibrated amino-acid
248 racemization (AAR) rates extending to MIS 5 (Kaufman et al., 2008; Adler et al., 2009), and coccolith
249 occurrences (Backman et al., 2009). The correlation is primarily based on sediment color and
250 distribution of Mn and Ca content showing a regionally consistent pattern (Fig. 5) (Polyak et al., 2009;
251 Stein et al., 2010; Schreck et al., 2018). According to ^{14}C dating, brown, Mn-rich units B1 and B2,
252 including the detrital carbonate layer W3, represent MIS 1 (~ 9 ka) and MIS 3 (34-45 ka)
253 interglacial/interstadial environments, respectively (Fig. 5; Table 2). The intermittent grey unit G1 thus

254 corresponds to the last glaciation/deglaciation (MIS 2 to 1) and the youngest, pre-glacial part of MIS 3.

255 Brown units B3 to B5 recovered by core 16B-GC have been attributed in the reference cores to
256 pre-MIS 3 interstadials ranging to MIS 5c, with some variance. Based on coccolith distribution in
257 HLY0503-8JPC, Backman et al. (2009) suggested that B5 represents MIS 5a, while Adler et al. (2009)
258 assigned its age to MIS 5c, consistent with AAR ages (Kaufman et al., 2008). This age model was also
259 used by Schreck et al. (2018), who pointed out that the coccolith stratigraphy cannot pinpoint a specific
260 time interval within MIS 5. In any case, core 16B-GC does not reach the prominent detrital carbonate
261 layer PW2 identified in multiple cores across the western Arctic Ocean, including HLY0503-8JPC (Fig.
262 5), and attributed to MIS 5d (e.g., Stein et al., 2010; Bazhenova et al., 2017; Dong et al., 2017). Overall,
263 we consider MIS 5c, with the approximate age of ca. 100 ka, as a reasonable estimate for the bottom of
264 16B-GC.

265 The developed lithostratigraphic framework indicates that a ~150-cm thick grey unit G2 pre-
266 dates the MIS 3 interstadial, likely being contained in the time interval from MIS 4 to early MIS 3. This
267 prominent lithostratigraphic unit can be traced in multiple cores from the Siberian margin to the Arctic
268 Ocean interior (e.g., Spielhagen et al., 2004; Polyak et al., 2009; Dong et al., 2017; Wang et al., 2018),
269 and has been proposed to correlate to the last pre-LGM glaciation in northern Eurasia with a glacial
270 maximum around 50-60 ka (Svendsen et al., 2004).

271 In comparison to this, regionally consistent age model, the B2 unit in a very similar nearby record
272 was assigned to MIS 5 based solely on the presence of rare coccoliths, including *E. huxleyi* (core
273 SWERUS-L2-13PC; <https://bolin.su.se/data/swerus/physical.php>; Fig. 1) (Jakobsson et al., 2016). The
274 occurrence of *E. huxleyi* clearly indicates that the sediments of this unit are younger than MIS 8/7
275 (Thiersten et al., 1977; Backman et al., 2009). However, due to an overall limited occurrence of
276 coccoliths, *E. huxleyi* presence may not be used to identify specific substages within MIS 5 as
277 attempted previously (e.g., Jakobsson et al., 2001; Spielhagen et al., 2004) because this species can
278 potentially occur in other relatively warm intervals of Arctic sediments. In particular, MIS 3 is a very
279 pronounced interstadial unit in Arctic paleoceanographic records, as exemplified by a high content of

280 Mn and high productivity indicated by abundant planktic and benthic microfossils (Nørgaard-Pedersen
281 et al., 1998; Adler et al., 2009; Hanslik et al., 2010; Schreck et al., 2018). Some authors further inferred
282 reduced sea ice and enhanced the advection of Atlantic waters during this time (Cronin et al., 2012;
283 Poirier et al., 2012). We note that in another SWERUS core from the Siberian margin further west, *E.*
284 *huxleyi* was also found in B2 with a ^{14}C age of 33 ka just a little above this finding (O'Regan et al.,
285 2017).

286

287 **5.2. Core-seismic correlation**

288 Distinct acoustic reflectors on seismic records can be formed by vertical changes in acoustic
289 impedance controlled by sediment density and p-wave velocity. Deep-sea Arctic Ocean sediments
290 generally consist of relatively soft fine-grained muds, which are occasionally intercalated with denser,
291 coarse sediment layers mostly attributed to iceberg sedimentation during deglacial events (Clark et al.,
292 1980; Polyak et al., 2009; Stein et al., 2010; Dong et al., 2017; Schreck et al., 2018). In particular,
293 detrital carbonate IRD layers, such as W3 and PW2 captured by western Arctic Ocean sediments, are
294 characterized in cores from the study region by a remarkably high density and p-wave velocity
295 compared to the enclosing fine-grained muds (Matthiessen et al., 2010; Stein et al., 2010; Schreck et
296 al., 2018). These layers, marking the LIS iceberg discharge from the Canadian Arctic, thus have the
297 potential to form strong reflectors.

298 Comparison of the subbottom acoustic reflection data and core 16B record (Fig. 6) confirms that
299 the surficial reflector R1 represents the seafloor, the interface between bottom water and relatively dense
300 surficial sediment of unit B1. A fine-grained unit G1 characterized by a relatively constant density and
301 p-wave velocity in multiple records from the study region (Matthiessen et al., 2010; Stein et al., 2010;
302 Schreck et al., 2018) defines a mostly transparent echo characteristic of SSU 1. A strong reflector R2
303 probably indicates a pronounced lithological change from the IRD-rich interval, including the W3 layer
304 to the overlying fine-grained unit G1 (Fig. 6). A relatively strong reflector in the uppermost part of SSU
305 2, partially divided into two layers, appears to be associated with a relatively coarse unit B2 (Fig. 6). A

306 transparent echo signature similar to that in SSU 1 characterizes the upper part of SSU 2 corresponding
307 to the fine-grained, thickest unit G2. Two thin reflectors of low to moderate amplitude in the lower part
308 of SSU 2 appear to correspond to a relatively sandy unit B3, especially its detrital carbonate-rich base
309 layer, and an intermittent sandy layer within G3 (Fig. 6). While core 16B-GC does not extend to the
310 depth of R3, a likely candidate for this strong reflector is a prominent, IRD-rich, detrital carbonate layer
311 PW2 that underlies unit B6 and is barely reached by 16B-GC (Fig. 5). PW2 is characterized by a
312 significantly higher wet bulk density and p-wave velocity than other Upper Quaternary sediments in
313 the study region (Mattiessen et al., 2010; Schreck et al., 2018).

314

315 **5.3. Glaciogenic debris lobes on the AP slope**

316 The presence of debris lobes in the lower part of SSU 2 up-slope from core 16B (Fig. 2) is likely
317 related to glacial scouring on the AP crest. While debris flows can potentially originate from various
318 slope instability processes, the consistent occurrence of these lobes in the Arctic Ocean downslope from
319 continental margins and plateaus characterized by glacial erosion/deposition indicates their glaciogenic
320 origin. In particular, the CB features debris lobes on both the AP and Chukchi Plateau slopes (Niessen
321 et al., 2013; Dove et al., 2014 and reference therein), indicating glaciogenic inputs from both sides. The
322 mechanisms for debris flows could include sediment bulldozing on the tops by grounded ice and/or
323 rapid deposition of deglacial sediments, e.g., from glacial underflows (e.g., Powell, 1990; Batchelor
324 and Dowdeswell, 2015). The timing of debris lobe emplacement would thus correspond to glacial
325 advance or early deglaciation stages.

326 The SSW-NNE orientation and southward inclination of the youngest set of glacial lineations
327 on the AP top indicate that the eroding ice was sourced from the East Siberian margin (Niessen et al.,
328 2013). According to the age constraints developed for core 16B-GC and a correlative core 28B-GC
329 from the AP top (Fig. 5), this event occurred prior to the MIS 3 interstadial and was possibly related to
330 a major glaciation in northern Siberia dated to the time interval between ~70 and 50 ka (Svendsen et
331 al., 2004; Möller et al., 2015).

332 The upper seismostratigraphic unit SSU 1 bounded by the seafloor, and the W3 layer represents
333 deposition during the time interval from late MIS 3 to the Holocene (Fig. 6). The absence of glaciogenic
334 debris lobes within SSU 1 indicates that glacial erosion of the AP was unlikely during the LGM, as
335 suggested in previous studies (Niessen et al., 2013; Schreck et al., 2018).

336

337 **5.4. Glacier-induced depositional environments**

338 Based on the developed age model, sedimentary unit G2 (MIS 4 to early MIS 3) that is
339 characterized by laminated mud facies, has a relatively high sedimentation rate of ~6 cm/kyr as
340 compared to more bioturbated units G3 and G4 (Fig. 4, Table 2). Laminated structures of glaciogenic
341 sediments in the high-latitude oceans can be potentially formed under various depositional settings such
342 as permanent sea ice, turbid meltwater plumes, distal fine-grained turbidity currents, and contour
343 currents (Hesse et al., 1996; Darby et al., 1997; Kleiber et al., 2000; ÓCofaigh et al., 2003; Matthiessen
344 et al., 2010). However, contour currents are unlikely to be strong in a semi-enclosed Arctic deep-sea
345 basin, while sedimentation rates under perennial sea ice are too low to form a laminated sedimentary
346 sequence. Couplets of TLm/TLs and Hm facies similar to those observed in 16B-GC (Fig. 4) have been
347 interpreted in previous studies as deposition from underflow turbidity currents in combination with
348 rapid settling from fine-grained suspension plumes in the attenuation stage of the carrying current (Piper,
349 1978; Chough, 1984; Yoon et al., 1991). The occurrence of TLm/TLs facies within G2 and G3 suggests
350 that turbidities could be associated with the glaciogenic debris flows emanating from their front on a
351 relatively steep AP slope (Fig. 2B). The development of CLm facies may reflect deposition from turbid
352 meltwater plumes repeatedly discharged from ice-sheet termini (Hesse et al., 1996; Kleiber et al., 2000;
353 ÓCofaigh et al., 2003).

354 Glacial erosion on glaciated continental margins plays an important role in delivering large
355 amounts of sediments to the continental slope and the adjacent basins, and thus leading to the formation
356 of debris flows (Vorren et al., 1998; Kleiber et al., 2000; Dowdeswell and Elverhøi, 2002; Jakobsson et
357 al., 2008). Based on our seismostratigraphic and sediment core data, this scenario applies to the AP

358 during MIS 4, when large volumes of eroded sediment may have been transported as proglacial under-
359 and overflows into the adjacent deep basin. This rapid sediment deposition likely caused slope
360 instability and thus triggered debris flows. Suspended fine sediments could have been detached from
361 the slope and transported into the interior of the Arctic Ocean at the density boundaries between
362 different water masses with subsequent deposition. Prolonged glacial erosion could have also formed
363 repeatedly detached turbid layers, leading to the formation of crudely laminated mud (CLm) facies (Fig.
364 7A). As the grounded ice retreated, turbid meltwater underflow plumes were likely repeatedly
365 discharged from the grounding line, thereby depositing CLm facies (Hesse et al., 1996; ÓCofaigh et al.,
366 2003) (Fig. 7B). These glacier-induced processes could lead to the deposition of fine-grained, fully
367 laminated sediments with fairly high sedimentation rates (unit G2) during the MIS 4 deglaciation that
368 may have extended to early MIS 3.

369 Bioturbated sediments of B2 and the overlying W3 layer are interpreted to represent hemipelagic
370 depositional environments with drifting icebergs during a relatively warm period of MIS 3 (Fig. 7C).
371 In general, Mn-enriched, brown sediments are believed to reflect elevated sea levels and/or reduced
372 sea-ice conditions, under which sediment from the Siberian shelves could be transported to the central
373 Arctic basins (Jakobsson et al., 2000; Polyak et al., 2004, 2009; Stein et al., 2010; Löwemark et al.,
374 2014; Ye et al., 2019). Overall, sedimentary properties of G2 and overlying facies indicate depositional
375 environments affected by the advance and retreat of a marine-based ice sheet grounded on the AP top.

376 The absence of glaciogenic debris lobe within SSU 1 indicates that the AP has not encountered
377 glacial erosion during MIS 2, consistent with previous studies from the Arctic Ocean off the Siberian
378 margin (Niessen et al., 2013; Schreck et al., 2018) as well as terrestrial studies from adjacent islands
379 and the East Siberian mainland (Romanovskii et al., 2004; Gualtieri et al., 2005). Nevertheless, the
380 presence of CLm facies within unit G1, most of which is attributed to MIS 2 (Figs. 3, 4), reflects glacier-
381 induced depositional processes, such as the suspension settling of turbid meltwater plumes and detached
382 turbid layers (Figs 7D, E). This lithology indicates the influence of a limited glaciation in the study
383 region, although its location and distribution pattern (e.g., grounded ice vs. ice shelf) needs to be further

384 investigated. There is no evidence for the LGM glaciation at the East Siberian margin, but data from
385 the eastern Chukchi shelf margin show glaciogenic bedforms indicative of grounded ice, age-
386 constrained to MIS 2 (Polyak et al., 2007). These bedforms are restricted to water depths of less than
387 ~450 m, but we cannot exclude that this grounded ice extended over the Chukchi shelf to its western
388 margin bordering the Chukchi Basin.

389 The predominance of the bioturbated sandy mud (Bsm) facies in the uppermost unit B1 reflects
390 hemipelagic deposition with sea-ice and/or iceberg debris rafting during much of the Holocene (Fig.
391 7F). Intense bioturbation indicates a relatively elevated export of primary production to the seafloor,
392 and thus moderate sea-ice conditions, and/or enhanced oxygenation of surface sediments.

393

394 **6. Conclusions**

395 A combination of litho- and seismostratigraphy on the basinward slope of the Arliss Plateau
396 depicts a glacier-induced depositional history in front of the East Siberian continental margin since
397 estimated MIS 5c (~100 ka). The age constraints were obtained by correlation of the studied core
398 ARA02B/16B-GC with earlier developed stratigraphies (Adler et al., 2009; Schreck et al., 2018). Based
399 on this age model and the core-seismic correlation, deposition of the youngest glaciogenic debris lobes
400 on the slope, indicative of the last glacial erosion of the AP top, occurred within seismostratigraphic
401 unit SSU 2 during MIS 4 to early MIS 3. This event may be correlative to a major glaciation in northern
402 Siberia that has been constrained to the time interval between ~70 and 50 ka (Svendsen et al., 2004;
403 Möller et al., 2015). Laminated sedimentary facies and sedimentation rates as high as ~6 cm/kyr in the
404 respective core interval (lithological unit G2) reflect glacier-induced sediment deposition. This
405 enhanced sedimentation probably resulted from detached turbid layers, turbidity currents, and
406 meltwater discharge pulses during glaciation/deglaciation.

407 The absence of glaciogenic debris lobes within the upper seismostratigraphic unit SSU 1 (late
408 MIS 3 to 1) indicates that glacial erosion unlikely impacted the AP during the LGM, consistent with

409 previous inferences (Niessen et al., 2013; Schreck et al., 2018). Nevertheless, the presence of laminated
410 facies within the corresponding core interval G1 may indicate a limited glaciation at a nearby
411 continental margin. Further investigation by geophysical seafloor surveys verified by sediment core
412 records is needed to better understand the glacial history of the western Arctic Ocean.

413

414 **Acknowledgments**

415 We want to thank the captain and crew of RV Araon for excellent collaboration and support
416 during the 2nd Arctic expedition ARA02B in 2011. This research is mainly funded by a seed-type
417 research project (PE19350 to S.I. Nam) of Korea Polar Research Institute. LP contribution was partially
418 supported by the US National Science Foundation award ARC-1304755. We thank an anonymous
419 reviewer and Matt O'Regan for detailed comments that helped to improve the manuscript.

420

421 **References**

- 422 Adler, R.E., Polyak, L., Ortiz, J.D., Kaufman, D.S., Channell, J.E.T., Xuan, C., Grottoli, A.G., Sellén,
423 E., Crawford, K.A., 2009. Sediment record from the western Arctic Ocean with an improved Late
424 Quaternary age resolution: HOTRAX core HLY0503-8JPC, Mendeleev Ridge. *Glob. Planet.*
425 *Change* 68, 18-29.
- 426 Backman, J., Fornaciari, E., Rio, D., 2009. Biochronology and paleoceanography of late Pleistocene
427 and Holocene calcareous nannofossil abundances across the Arctic Basin. *Marine*
428 *Micropaleontology* 72, 86-98.
- 429 Batchelor, C.L., Dowdeswell, J.A., 2014. The physiography of High Arctic cross-shelf troughs. *Quat.*
430 *Sci. Rev.* 92, 68-96.
- 431 Batchelor, C.L., Dowdeswell, J.A., 2015. Ice-sheet grounding-zone wedges (GZWs) on high-latitude
432 continental margins. *Marine Geology*, 363: 65-92
- 433 Bazhenova, E., Fagel, N., Stein, R., 2017. North American origin of “pink–white” layers at the
434 Mendeleev Ridge (Arctic Ocean): New insights from lead and neodymium isotope composition of

435 detrital sediment component. *Mar. Geol.* 386, 44-55.

436 Bischof, J.F., Darby, D.A., 1997. Mid-to Late Pleistocene ice drift in the western Arctic Ocean:
437 evidence for a different circulation in the past. *Science* 277, 74-78.

438 Chough, S., 1984. Fine-grained turbidites and associated mass-flow deposits in the Ulleung (Tsushima)
439 Back-arc Basin, East Sea (Sea of Japan). *Geol. Soc. London Spec. Publ.* 15, 185-196.

440 Clark, D.L., Whitman, R.R., Morgan, K.A., Mackey, S.D., 1980. Stratigraphy and glacial-marine
441 sediments of the Amerasian Basin, central Arctic Ocean. Geological Society of America.

442 Cronin, T.M., Dwyer, G.S., Farmer, J., Bauch, H.A., Spielhagen, R.F., Jakobsson, M., Nilsson, J.,
443 Briggs Jr, W., Stepanova, A., 2012. Deep Arctic Ocean warming during the last glacial cycle. *Nature*
444 *Geoscience* 5, 631. Darby, D.A., Bischof, J.F., Jones, G.A., 1997. Radiocarbon chronology of
445 depositional regimes in the western Arctic Ocean. *Deep Sea Research Part II: Topical Studies in*
446 *Oceanography* 44, 1745-1757.

447 Dong, L., Liu, Y., Shi, X., Polyak, L., Huang, Y., Fang, X., Liu, J., Zou, J., Wang, K., Sun, F., Wang,
448 X., 2017. Sedimentary record from the Canada Basin, Arctic Ocean: implications for late to middle
449 Pleistocene glacial history. *Clim. Past* 13, 511-531.

450 Dove, D., Polyak, L., Coakley, B., 2014. Widespread, multi-source glacial erosion on the Chukchi
451 margin, Arctic Ocean. *Quat. Sci. Rev.* 92, 112-122.

452 Dowdeswell, J.A., Elverhøi, A., 2002. The timing of initiation of fast-flowing ice streams during a
453 glacial cycle inferred from glacial marine sedimentation. *Mar. Geol.* 188, 3-14.

454 England, J.H., Furze, M.F., Douppé, J.P., 2009. Revision of the NW Laurentide Ice Sheet: implications
455 for paleoclimate, the northeast extremity of Beringia, and Arctic Ocean sedimentation. *Quat. Sci.*
456 *Rev.* 28, 1573-1596.

457 Grobe, H., 1987. A simple method for the determination of ice-rafted debris in sediment cores.
458 *Polarforschung* 57, 123-126.

459 Gualtieri, L., Vartanyan, S., Brigham-Grette, J., Anderson, P., 2005. Evidence for an ice-free Wrangel
460 Island, northeast Siberia during the Last Glacial Maximum. *Boreas* 34, 264-273.

461 Hanslik, D., Jakobsson, M., Backman, J., Björck, S., Sellén, E., O'Regan, M., Fornaciari, E., Skog, G.,

462 2010. Pleistocene Arctic Ocean sea ice and deep water isolation times. *Quat. Sci. Rev* 29, 3430-
463 3441.

464 Hesse, R., Klauke, I., Ryan, W.B., Edwards, M.B., Piper, D.J.W., 1996. Imaging Laurentide Ice Sheet
465 Drainage into the Deep Sea: Impact on Sediments and Bottom Water. *Oceanographic Literature*
466 *Review* 4.

467 Jakobsson, M., Andreassen, K., Bjarnadóttir, L.R., Dove, D., Dowdeswell, J.A., England, J.H., Funder,
468 S., Hogan, K., Ingólfsson, Ó., Jennings, A., Krog Larsen, N., Kirchner, N., Landvik, J.Y., Mayer,
469 L., Mikkelsen, N., Möller, P., Niessen, F., Nilsson, J., O'Regan, M., Polyak, L., Nørgaard-Pedersen,
470 N., Stein, R., 2014. Arctic Ocean glacial history. *Quat. Sci. Rev.* 92, 40-67.

471 Jakobsson, M., Grantz, A., Kristoffersen, Y., Macnab, R., 2003. Physiographic provinces of the Arctic
472 Ocean seafloor. *Geol. Soc. Am. Bull.* 115.

473 Jakobsson, M., Løvlie, R., Al-Hanbali, H., Arnold, E., Backman, J., Mörth, M., 2000. Manganese and
474 color cycles in Arctic Ocean sediments constrain Pleistocene chronology. *Geology* 28, 23-26.

475 Jakobsson, M., Løvlie, R., Arnold, E., Backman, J., Polyak, L., Knutsen, J.-O., Musatov, E., 2001.
476 Pleistocene stratigraphy and paleoenvironmental variation from Lomonosov Ridge sediments,
477 central Arctic Ocean. *Glob. Planet. Change* 31, 1-22.

478 Jakobsson, M., Nilsson, J., Anderson, L., Backman, J., Björk, G., Cronin, T.M., Kirchner, N.,
479 Koshurnikov, A., Mayer, L., Noormets, R., O'Regan, M., Stranne, C., Ananiev, R., Barrientos
480 Macho, N., Cherniykh, D., Coxall, H., Eriksson, B., Flodén, T., Gemery, L., Gustafsson, Ö., Jerram,
481 K., Johansson, C., Khortov, A., Mohammad, R., Semiletov, I., 2016. Evidence for an ice shelf
482 covering the central Arctic Ocean during the penultimate glaciation. *Nature Communications* 7,
483 10365.

484 Jakobsson, M., Polyak, L., Edwards, M., Kleman, J., Coakley, B., 2008. Glacial geomorphology of the
485 Central Arctic Ocean: the Chukchi Borderland and the Lomonosov Ridge. *Earth Surf. Proc. Land.*
486 33, 526-545.

487 Jokat, W., 2008. The expedition of the research vessel "Polarstern" to the Arctic in 2008 (ARK-XXIII/3).

488 Kaufman, D.S., Polyak, L., Adler, R., Channell, J.E., Xuan, C., 2008. Dating late Quaternary planktonic

489 foraminifer *Neogloboquadrina pachyderma* from the Arctic Ocean using amino acid racemization.
490 *Paleoceanography* 23.

491 Kleiber, H., Knies, J., Niessen, F., 2000. The Late Weichselian glaciation of the Franz Victoria Trough,
492 northern Barents Sea: ice sheet extent and timing. *Mar. Geol.* 168, 25-44.

493 Löwemark, L., März, C., O'Regan, M., Gyllencreutz, R., 2014. Arctic Ocean Mn-stratigraphy: genesis,
494 synthesis and inter-basin correlation. *Quat. Sci. Rev.* 92, 97-111.

495 Löwemark, L., O'Regan, M., Hanebuth, T., Jakobsson, M., 2012. Late Quaternary spatial and temporal
496 variability in Arctic deep-sea bioturbation and its relation to Mn cycles. *Paleogeogr. Paleoclimatol.*
497 *Paleoecol.* 365, 192-208.

498 März, C., Stratmann, A., Matthiessen, J., Meinhardt, A.K., Eckert, S., Schnetger, B., Vogt, C., Stein,
499 R., Brumsack, H.J., 2011. Manganese-rich brown layers in Arctic Ocean sediments: Composition,
500 formation mechanisms, and diagenetic overprint. *Geochimica et Cosmochimica Acta* 75, 7668-7687.

501 Matthiessen, J., Niessen, F., Stein, R., Naafs, B.D.A., 2010. Pleistocene glacial marine sedimentary
502 environments at the eastern Mendeleev Ridge, Arctic Ocean. *Polarforschung* 79, 123-137.

503 Möller, P., Alexanderson, H., Funder, S., Hjort, C., 2015. The Taimyr Peninsula and the Severnaya
504 Zemlya archipelago, Arctic Russia: a synthesis of glacial history and palaeo-environmental change
505 during the Last Glacial cycle (MIS 5e–2). *Quat. Sci. Rev.* 107, 149-181.

506 Niessen, F., Hong, J.K., Hegewald, A., Matthiessen, J., Stein, R., Kim, H., Kim, S., Jensen, L., Jokat,
507 W., Nam, S.-I., 2013. Repeated Pleistocene glaciation of the East Siberian continental margin.
508 *Nature Geoscience* 6, 842.

509 Nørgaard-Pedersen, N., Spielhagen, R.F., Thiede, J., Kassens, H., 1998. Central Arctic surface ocean
510 environment during the past 80,000 years. *Paleoceanography* 13, 193-204.

511 O'Regan, M., Backman, J., Barrientos, N., Cronin, T.M., Gemery, L., Kirchner, N., Mayer, L.A.,
512 Nilsson, J., Noormets, R., Pearce, C., 2017. The De Long Trough: a newly discovered glacial trough
513 on the East Siberian continental margin. *Clim. Past* 13, 1269.

514 ÓCofaigh, C., Taylor, J., Dowdeswell, J.A., Pudsey, C.J., 2003. Palaeo-ice streams, trough mouth fans
515 and high-latitude continental slope sedimentation. *Boreas* 32, 37-55.

516 Phillips, L. R., Grantz, A., 1997. Quaternary history of sea ice and paleoclimate in the Amerasia basin,
517 Arctic Ocean, as recorded in the cyclical strata of Northwind Ridge. *Geol. Soc. Am. Bull.* 109,
518 1101-1115.

519 Piper, D.W., 1978. Turbidite muds and silts on deepsea fans and abyssal plains. In Stanley, D.J. and
520 Kelling, G. (eds.), *Sedimentation in submarine canyons, fans, and trenches*, Hutchinson and Ross
521 Stroudsburg, 163-176.

522 Poirier, R.K., Cronin, T.M., Briggs Jr, W.M., Lockwood, R., 2012. Central Arctic paleoceanography
523 for the last 50 kyr based on ostracode faunal assemblages. *Marine Micropaleontology* 88, 65-76.

524 Polyak, L., Bischof, J., Ortiz, J.D., Darby, D.A., Channell, J.E.T., Xuan, C., Kaufman, D.S., Løvlie, R.,
525 Schneider, D.A., Eberl, D.D., Adler, R.E., Council, E.A., 2009. Late Quaternary stratigraphy and
526 sedimentation patterns in the western Arctic Ocean. *Glob. Planet. Change* 68, 5-17.

527 Polyak, L., Curry, W.B., Darby, D.A., Bischof, J., Cronin, T.M., 2004. Contrasting glacial/interglacial
528 regimes in the western Arctic Ocean as exemplified by a sedimentary record from the Mendeleev
529 Ridge. *Paleogeogr. Paleoclimatol. Paleoecol.* 203, 73-93.

530 Polyak, L., Darby, D.A., Bischof, J.F., Jakobsson, M., 2007. Stratigraphic constraints on late
531 Pleistocene glacial erosion and deglaciation of the Chukchi margin, Arctic Ocean. *Quat. Res.* 67,
532 234-245.

533 Powell, R.D., 1990, Glacimarine processes at grounding-line fans and their growth to ice-contact deltas,
534 in Dowdeswell, J.A., and Scourse, J.D., eds., *Glacimarine Environments: Processes and Sediments:*
535 *Geological Society of London Special Publication* 53, p. 53–73.

536 Romanovskii, N., Hubberten, H.-W., Gavrillov, A., Tumskey, V., Kholodov, A., 2004. Permafrost of
537 the east Siberian Arctic shelf and coastal lowlands. *Quat. Sci. Rev.* 23, 1359-1369.

538 Schreck, M., Nam, S.-I., Polyak, L., Vogt, C., Kong, G.S., Stein, R., Matthiessen, J., Niessen, F., 2018.
539 Improved Pleistocene sediment stratigraphy and paleoenvironmental implications for the western
540 Arctic Ocean off the East Siberian and Chukchi margins. *arktos* 4.

541 Spielhagen, R.F., Baumann, K.-H., Erlenkeuser, H., Nowaczyk, N.R., Nørgaard-Pedersen, N., Vogt,
542 C., Weiel, D., 2004. Arctic Ocean deep-sea record of northern Eurasian ice sheet history. *Quat. Sci.*

543 Rev. 23, 1455-1483.

544 Stein, R., Matthiessen, J., Niessen, F., Krylov, A., Nam, S.-I., Bazhenova, E., 2010. Towards a better
545 (litho-) stratigraphy and reconstruction of Quaternary paleoenvironment in the Amerasian Basin
546 (Arctic Ocean). *Polarforschung* 79, 97-121.

547 Stokes, C., Margold, M., Clark, C., Tarasov, L., 2016. Ice stream activity scaled to ice sheet volume
548 during Laurentide Ice Sheet deglaciation. *Nature* 530, 322.

549 Svendsen, J., 2004. Late Quaternary ice sheet history of northern Eurasia. *Quat. Sci. Rev.* 23, 1229-
550 1271. Thierstein, H., Geitzenauer, K., Molfino, B., Shackleton, N., 1977. Global synchronicity of late
551 Quaternary coccolith datum levels Validation by oxygen isotopes. *Geology* 5, 400-404.

552 Vorren, T.O., Laberg, J.S., F., B., Dowdeswell, J.A., N.H., K., J., M., J., R., Werner, F., 1998. The
553 Norwegian-Greenland Sea Continental Margins: Morphology and Late Quaternary Sedimentary
554 Processes and Environment. *Quat. Sci. Rev.* 17, 273-302.

555 Wang, R., Polyak, L., Xiao, W., Wu, L., Zhang, T., Sun, Y., Xu, X., 2018. Late-Middle Quaternary
556 lithostratigraphy and sedimentation patterns on the Alpha Ridge, central Arctic Ocean: Implications
557 for Arctic climate variability on orbital time scales. *Quat. Sci. Rev.* 181, 93-108.

558 Wang, R., Xiao, W., März, C., Li, Q., 2013. Late Quaternary paleoenvironmental changes revealed by
559 multi-proxy records from the Chukchi Abyssal Plain, western Arctic Ocean. *Glob. Planet. Change*
560 108, 100-118.

561 Ye, L., März, C., Polyak, L., Yu, X., Zhang, W., 2019. Dynamics of manganese and cerium enrichments
562 in Arctic Ocean sediments: a case study from the Alpha Ridge. *Frontiers in Earth Science* 6.

563 Yoon, S., Chough, S., Thiede, J., Werner, F., 1991. Late Pleistocene sedimentation on the Norwegian
564 continental slope between 67 and 71 N. *Mar. Geol.* 99, 187-207.

565

566

567

568

569

570 **Figure and Table captions**

571 **Figure 1** (A) Index physiographic map of the study area showing the location of cores ARA02B/16B-
572 GC (this study), ARA03B/28B-GC (Schreck et al., 2018) and HLY0503-8JPC (Adler et al., 2009). MR,
573 Mendeleev Ridge; AP, Arliss Plateau; CB, Chukchi Basin; CP, Chukchi Plateau; NR, Northwind Ridge.
574 Solid line tracks sub-bottom profiler data. Bathymetric contour interval is 250 m. (B) Broader
575 physiographic/paleogeographic context with inferred ice-sheet maxima shown by semi-transparent
576 white fill (Svendsen et al., 2004; Niessen et al., 2013; Stokes et al., 2016). (C) Multibeam bathymetry
577 of the Arliss Plateau showing several generations of Mega-Scale Glacial Lineations. Bathymetric
578 contour interval is 100 m.

579 **Figure 2** Sub-bottom profiler from Arliss Plateau to Chukchi Basin across the site of core
580 ARA02B/16B-GC (red vertical bar in panel B). Seismostratigraphic units SSU 1 and 2 are bounded by
581 distinct reflectors R1 to 3. The uppermost glaciogenic debris lobes on the slope are correlated with the
582 lower part of SSU 2. Black box shows the position of Fig. 6.

583 **Figure 3** Down-core distribution of sediment lightness (L^*), Mn/Al and Ca/Al ratios, IRD numbers,
584 and grain size in core ARA02B/16B-GC. Top 10 cm are estimated to be missing due to overpenetration;
585 XRF data for this interval (blue-colored solid lines) are spliced from the box core 16B-BC. High Mn/Al
586 and Ca/Al ratios in surficial sediment may be partially due to high water content (Thallinghii et al.,
587 2007). Lithostratigraphic indices are shown in Fig. 3.

588 **Figure 4** Split-core photos, X-radiograph images, and sedimentary facies (see Table 1 for details).
589 Indices for lithological units (B1-B5 and G1-G4) and the detrital carbonate layer W3 are shown on the
590 core photo.

591 **Figure 5** Lithostratigraphic correlation of core ARA02B/16B-GC with ARA03B/28B-GC (Schreck et
592 al., 2018) and HLY0503-8JPC (Adler et al., 2009) based on sediment color and variations of Mn/Al
593 and Ca/Al. The tops of major brown units (B2-B5) are correlated by dotted lines; the bottom of core

594 ARA03B/28B-GC is projected onto ARA02B/16B-GC by the dashed line. Estimated Marine Isotope
595 Stages and radiocarbon/AAR ages (Adler et al., 2009) are shown next to core HLY0503-8JPC.

596 **Figure 6** Correlation of the subbottom data with core ARA02B/16B-GC. Surficial reflector R1 is the
597 seafloor. Strong reflectors R2 and R3 correspond to prominent lithological changes at the boundaries
598 of fine-grained sediments and IRD-rich layers W3 and PW2. Estimated Marine Isotope Stages are
599 shown on the right.

600 **Figure 7** Schematic model of sedimentary processes on the Arliss Plateau and adjacent Chukchi Basin
601 during major depositional regimes from the MIS 4 glaciation to the Holocene.

602

603 **Table 1** Summary of sedimentary facies in core ARA02B/16B-GC. Black arrows indicate the intervals
604 of TLM, TLs, and Hm facies. See Fig. 4 for the stratigraphic distribution of sedimentary facies.

605 **Table 2** Estimated duration and sedimentation rates of lithostratigraphic units in core ARA02B/16B-
606 GC based on the age model developed from lithostratigraphic correlations (Fig. 5).

Figure 1

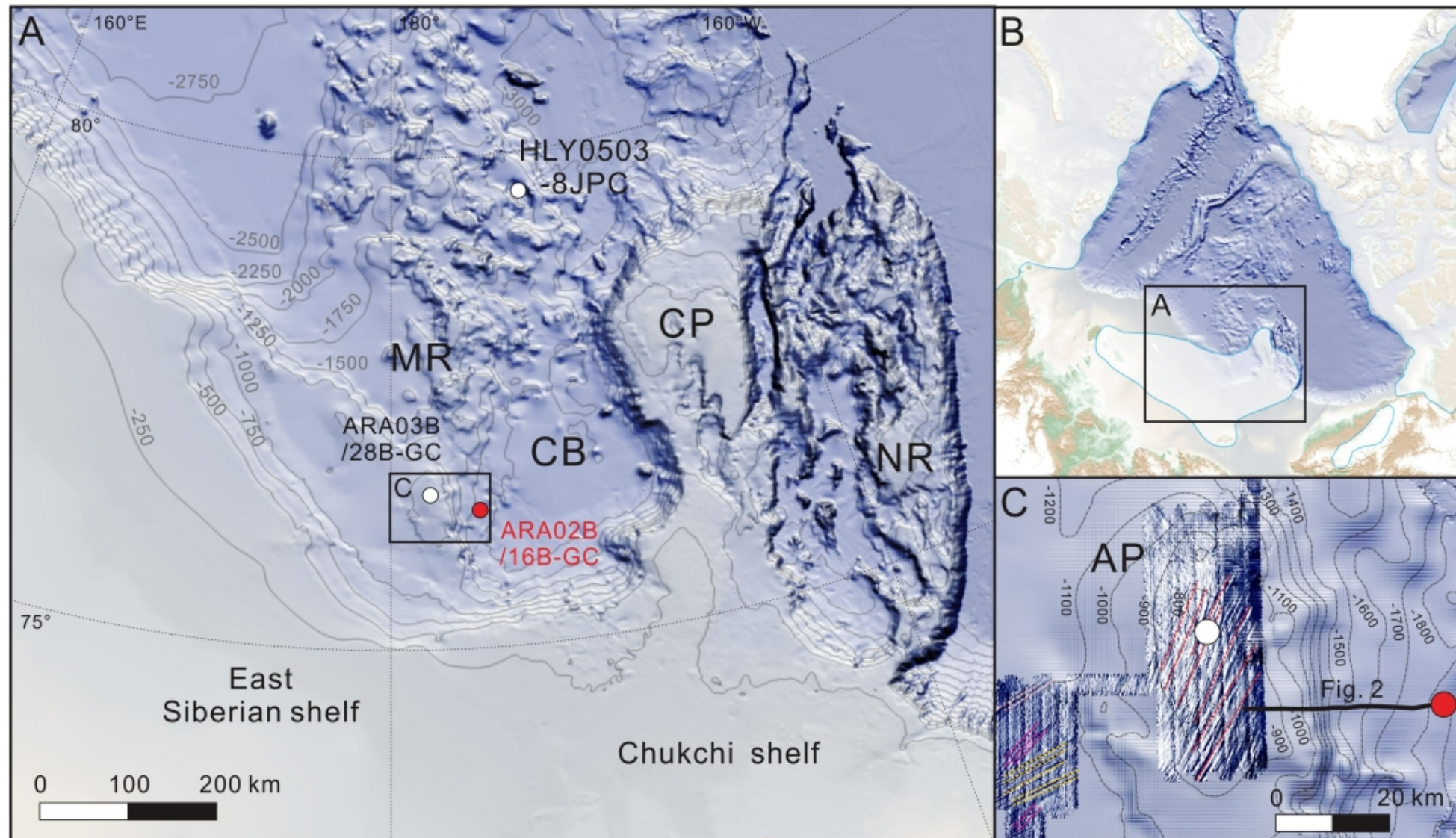


Figure 2

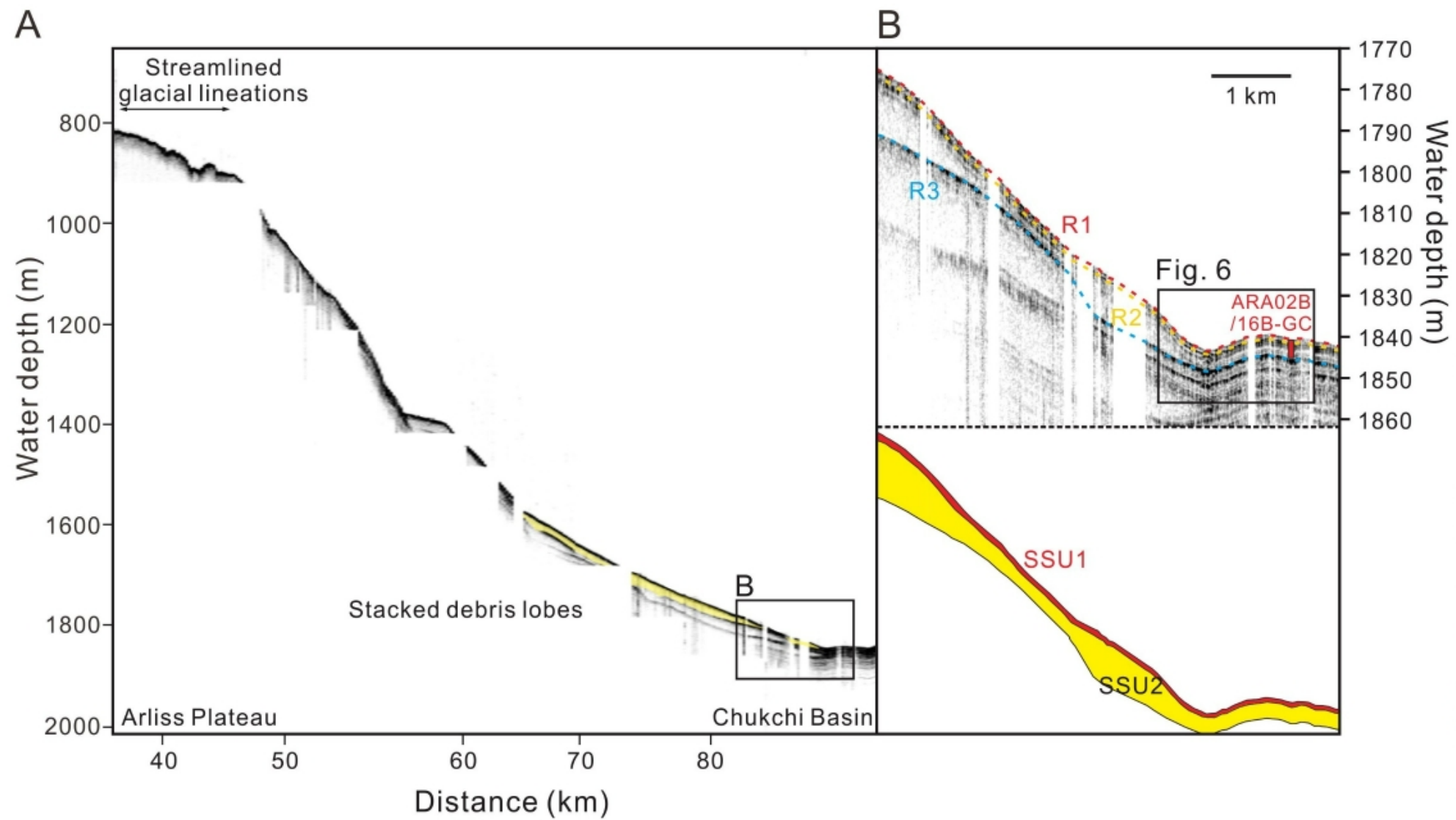


Figure 3

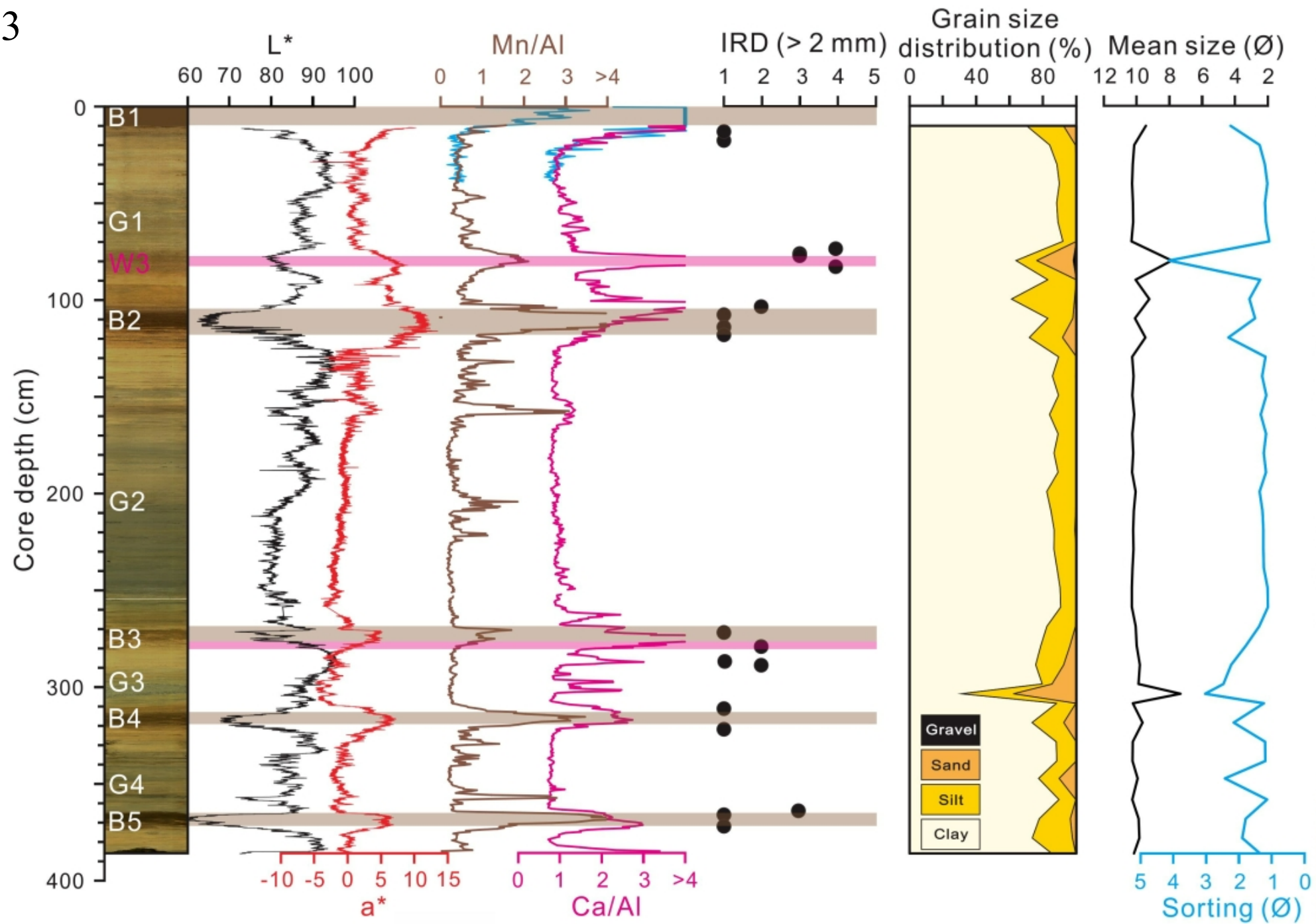


Figure 4

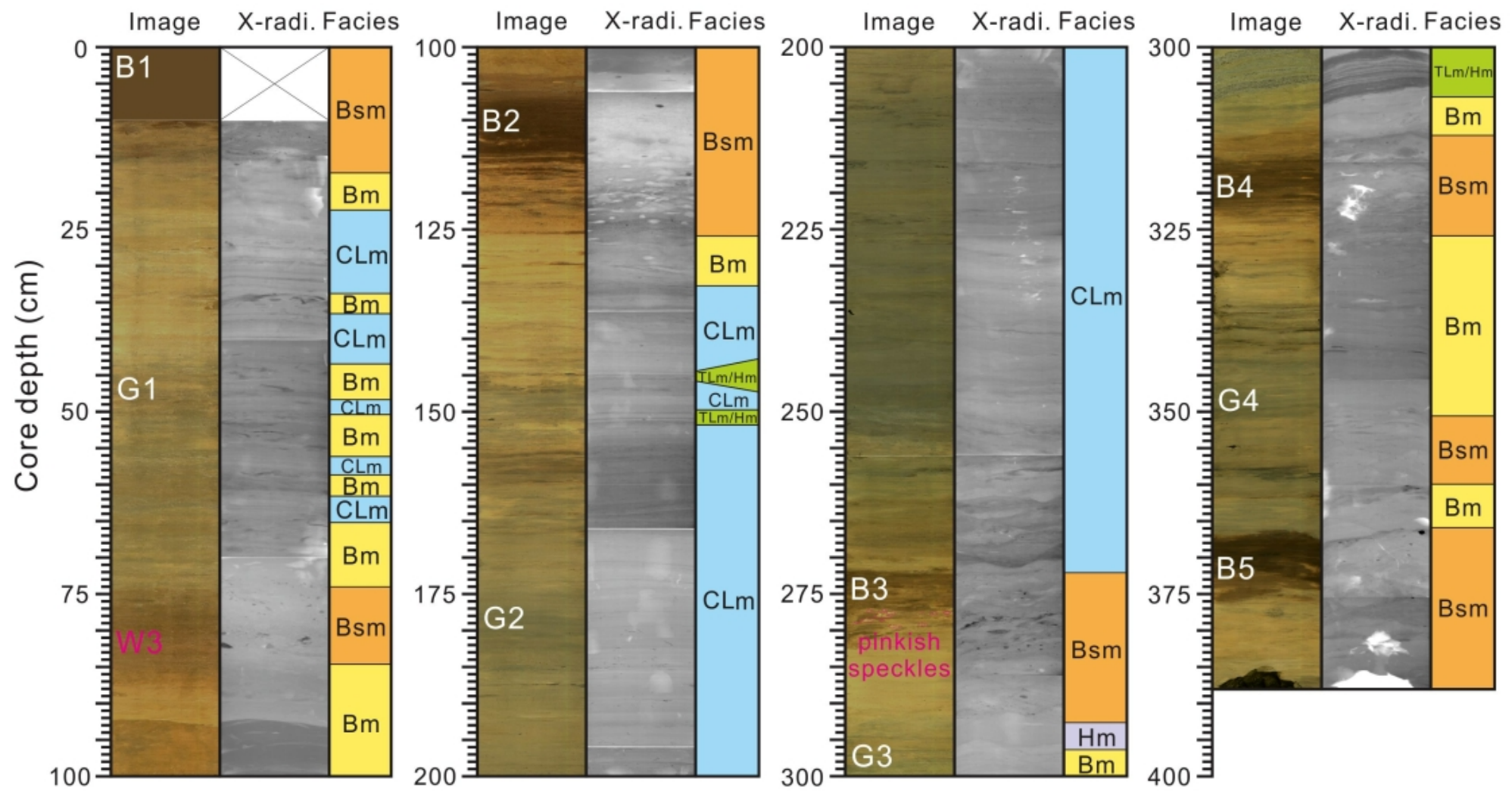


Figure 5

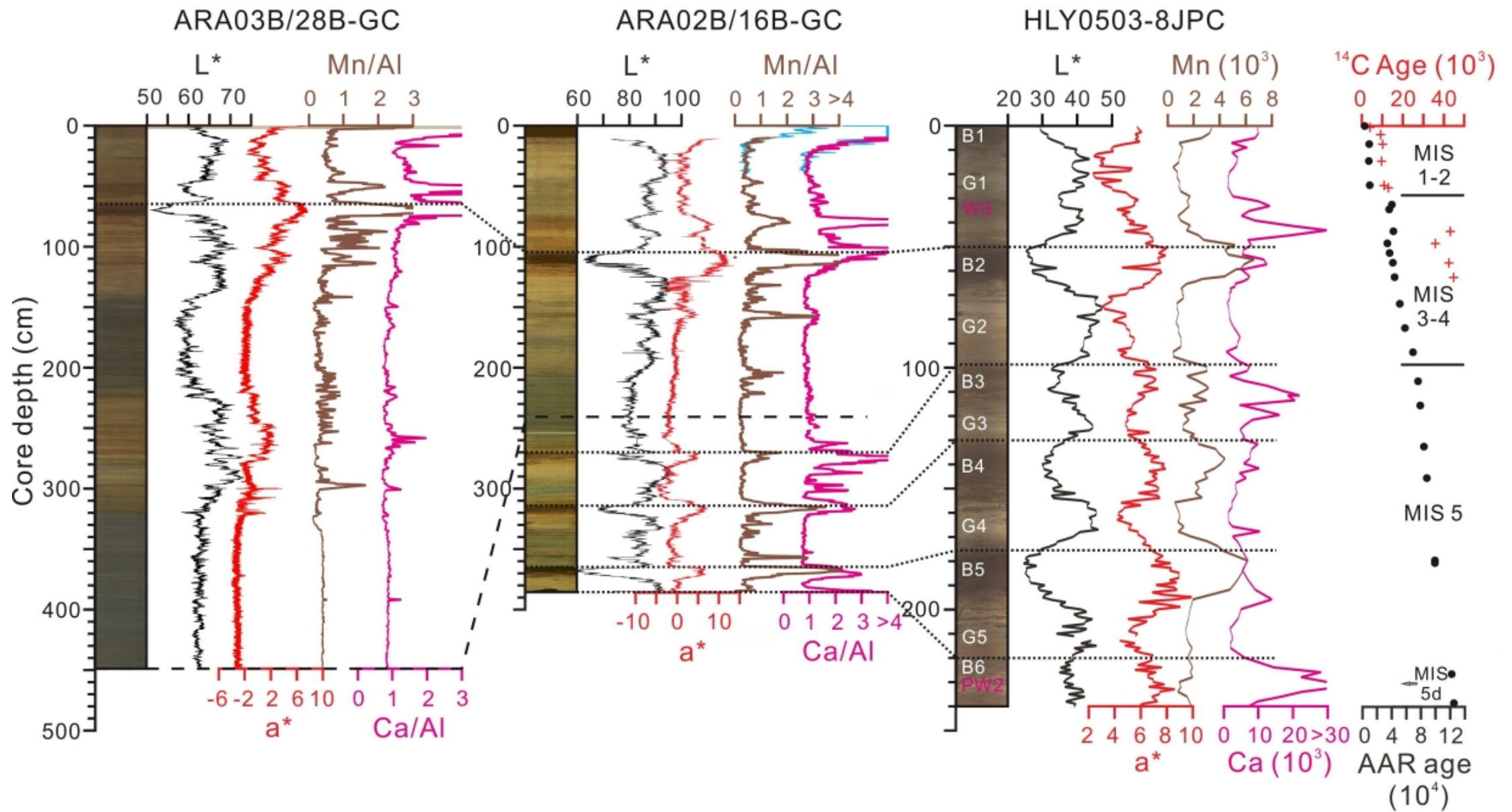


Figure 6

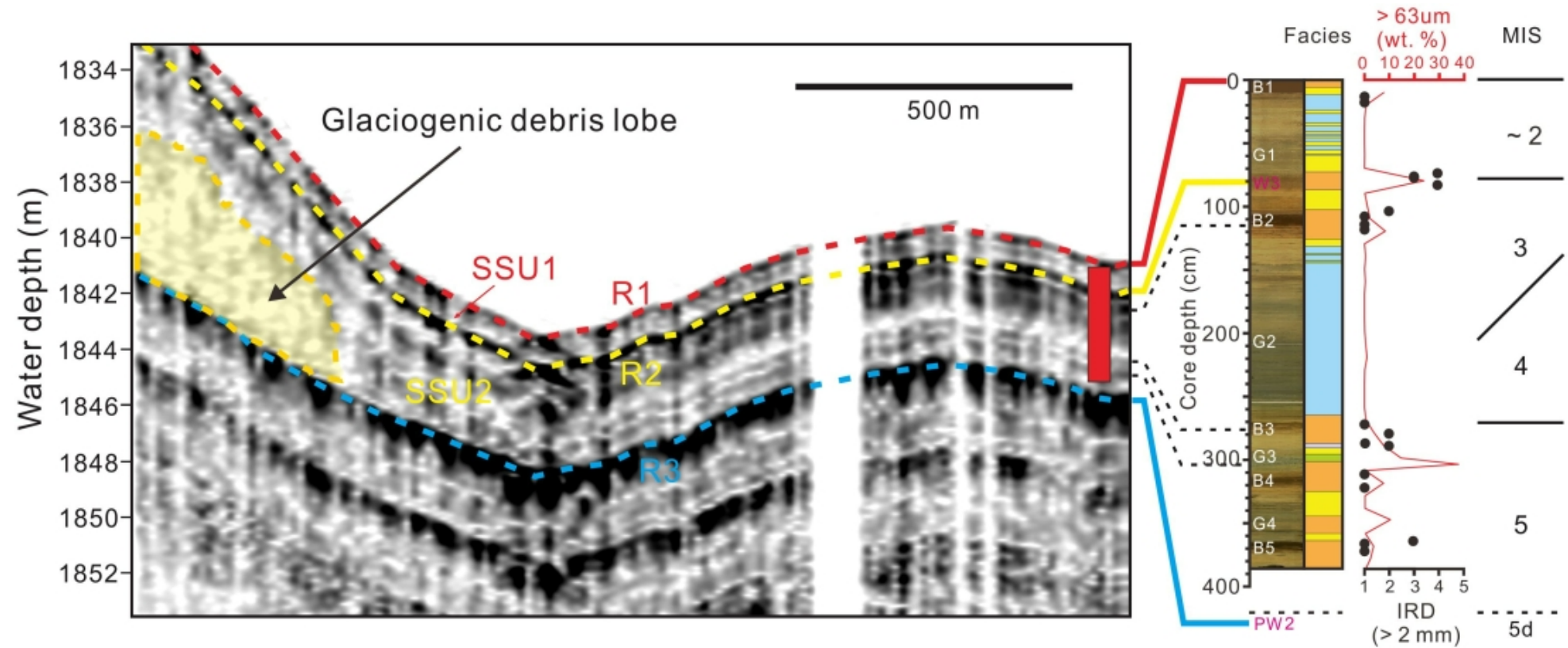
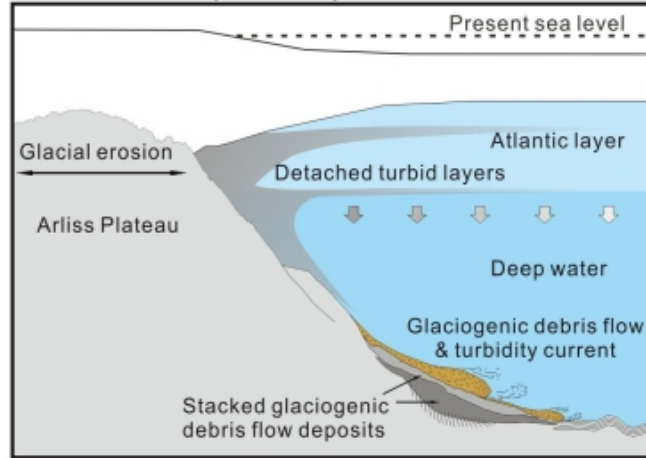
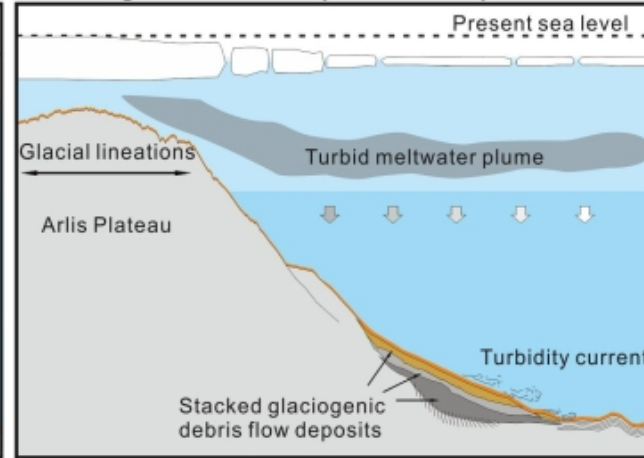


Figure 7

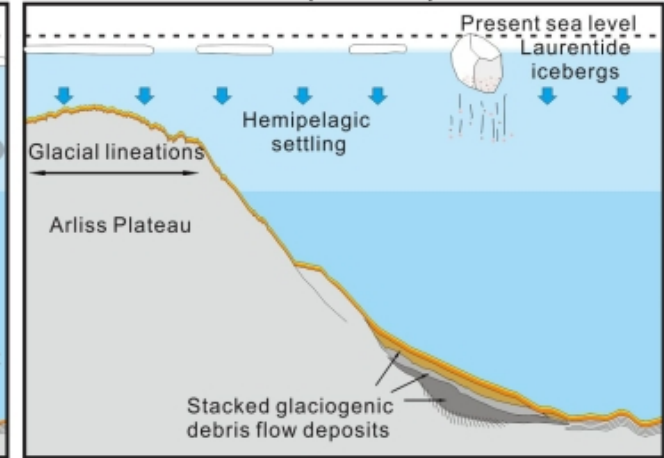
A. Stadial (MIS 4)



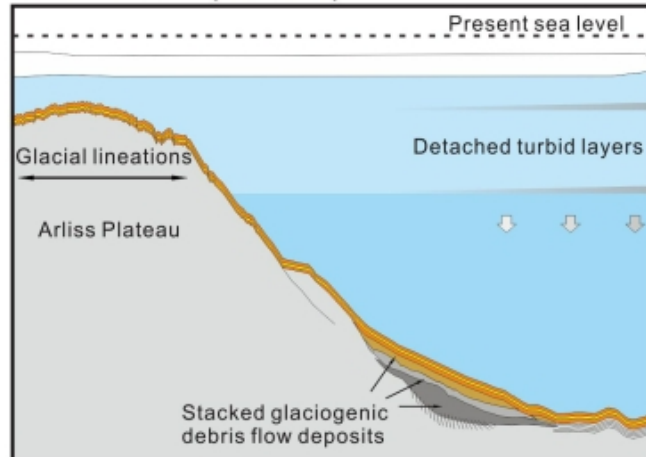
B. Deglaciation (MIS 3-4)



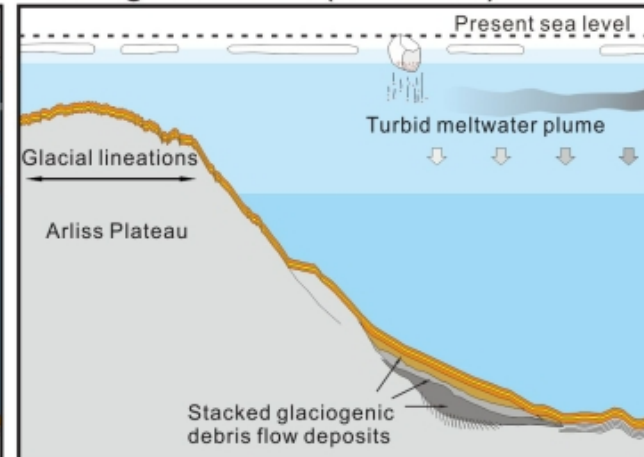
C. Interstadial (MIS 3)



D. Glacial (MIS 2)



E. Deglaciation (MIS 1-2)



F. Interglacial (MIS 1)

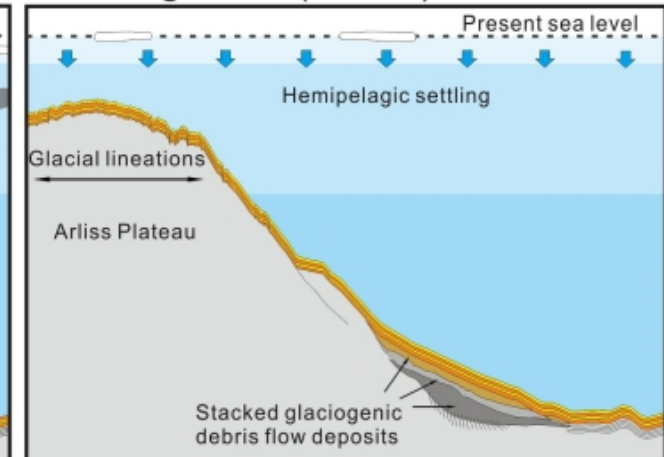


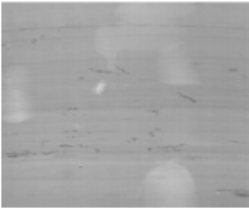
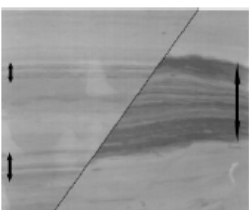
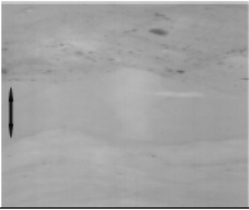


Table 1

| Facies | Description | Depositional process | |
|--|---|---|--|
| Bioturbated sandy mud (Bsm) |  | Brown to dark brown and pinkish; (gravelly) sandy mud, IRD-rich; very poorly sorted; intensely bioturbated, absence of primary structure; relatively sharp and flat upper boundaries and mottled lower basal contact | Hemipelagic settling affected by drifting ice (iceberg/sea-ice) |
| Bioturbated mud (Bm) |  | Yellow to olive grey; fine-grained mud, IRD is rare or absent; poorly sorted; located near brown and pinkish layers, repeatedly alternated with poorly defined laminated facies; gradual facies boundaries | Hemipelagic settling |
| Crudely laminated or layered mud (CLm) |  | Yellow to olive grey; silty mud to clayey mud, IRD is absent; poorly sorted; weakly bioturbated, planar and sub-parallel lamina or layers, lamination is laterally discontinuous and poorly defined, clayey lamina or layer is thicker (4-12 mm) than silty lamina (1-3 mm), non-systematic vertical changes, gradual facies boundaries | Repeated settling of suspension from turbid melt water plumes and/or detached turbid layers |
| Thinly laminated mud/sand (TLm/TLs) |  | Olive grey; silt-rich mud/sandy mud; IRD is absent; distinct and laterally continuous laminae are coupled with homogenous muds, relatively regular lamina thickness (1-3 mm), sharp lower boundaries and gradational upper boundaries | Bottom-hugging turbidity current |
| Homogeneous mud (Hm) |  | Olive grey; fine-grained mud, IRD is absent; poorly sorted; absence of primary structure as well as any grading and bioturbation; generally coupled with TLm/TLs facies | Rapid settling from fine-grained suspension plumes in the weakening stage of turbidity current |

Black arrows indicate each facies (TLm, TLs, and Hm)

Table 2

| Lithostratigraphy | Thickness (cm) | Duration (kyr) | Sedimentation Rate (cm/kyr) |
|--------------------------|---------------------------|---------------------------|--|
| B1 | 10 (0-10) | 9 (0-9) | 0.83 |
| G1 | 68 (10-78) | 25 (9-34) | 2.72 |
| W3-B2 | 37 (78-115) | 11 (34-45) | 3.36 |
| G2 | 157 (115-272) | 26 (45-71) | 6.04 |
| B3-B5 | 103 (272-375) | 25 (71-96) | 4.12 |